The impact of climate change and topography on spatial and temporal NPP dynamics using time-series Landsat data coupled with Biome-BGC model

Tuo Feng

A thesis
submitted in partial fulfillment of the
requirements for the degree of:

Master of Science

University of Washington
2019

Committee:
Daniel Vogt, chair
L. Monika Moskal
Stephan Gmur

Program authorized to offer degree:
School of Environmental and Forest Sciences

University of Washington

Abstract

The impact of climate change and topography on spatial and temporal NPP dynamics using time-series Landsat data coupled with Biome-BGC model

Tuo Feng

Chair of the Supervisory Committee:

Daniel Vogt

School of Environmental and Forest Sciences

Understanding the trends and variations of total ecosystem net primary productivity (NPP) is critical for simulating and predicting changes in the terrestrial carbon cycle across a range of spatial and temporal scales. A unique location to assist with enhancing our understanding of NPP is found in one of the largest temperate rainforests in the United States (US). It is a forest with one of the biggest carbon sinks in the US and is located in the Olympic Peninsula. In this study, four different models (Biome-BGC, Carnegie Ames Stanford Approach, Thornthwaite Memorial model and Miami model) were used to estimate mean annual NPP between the years 1986 to 2017 in two watersheds (Hoh and Queets) located on the Olympic Peninsula of Washington State. The spatial-temporal changes in NPP were correlated with climatic factors, topography and forest stand age. Spatially, annual NPP was estimated to be higher in the northwestern Hoh

watershed versus that found in the southeastern Queets watershed. This was likely due to differences in forest structure and species composition. In the two watersheds, the models suggested a general trend of NPP levels increasing with stand age. During that time period, two potential Turning Points (significant changes in NPP) were detected in the years 1997 and 2007. These NPP Turning Points (i.e., NPP increases) occurred after severe droughts. Results from this study showed predicted NPP levels being highly correlated to climatic factors. In fact, three of the models predicting NPP were very sensitive to changes in mean annual temperatures. Topographic effects on NPP were analyzed using the Topographic Solar Radiation Index (TSRI) acquired from the national digital elevation model (DEM) and airborne light detection and ranging (LiDAR) data. Changes in NPP estimates using LiDAR-based TSRI resulted in significant R^2 values of 0.59 for deciduous forests, 0.38 for evergreen forests, and 0.64 for mixed-forest composition. In this study region, forest stand successional stage was explained by forest disturbance and recovery history. Finally, three empirical functions were developed to describe the relationship between forest stand age and NPP levels, in terms of the different forest types. This study provides valuable information to assess the potential drivers of changes in carbon sequestration rates under dynamic climatic fluctuations in the Olympic Peninsula. It also highlights the significance of using solar radiation energy as a tool to estimate changes in forest productivity at a watershed scale.

Key words: NPP; Landsat; Biome-BGC; Stand age; TSRI; LiDAR; Climate, Olympic Peninsula

Table of Contents

List of Figures

List of Tables

Acknowledgements

Firstly, I hope to thank my advisor, Daniel Vogt. Your support and encouragement throughout this project have not only educated me how to act as an outstanding researcher, but also helped me to grow as an individual. I would also like to thank to my committee members, L. Monika Moskal and Stephan Gmur. It was impossible for me to finish this work without your constant help and guidance.

I definitely want to thank my parents, Yongwei Feng and Xuezhen Chen. I would not have had the opportunity to purse my graduate education without their motivation and encouragement, and, of course, for their financial support!

During my studies at the University of Washington in the School of Environmental and Forest Sciences (SEFS), I received much help from my professors, family members, SEFS staffs and friends. I want to express my sincere thanks to all of you, and especially:

Brian Harvey
David Campbell
Guang Zheng
Hao Liu
Jingyu Hu
Korena Mafune
Kristiina Vogt
Michelle Trudeau
Mingshi Li
Patricia Roads
Pinghao Li
Xuezhen Chen
Yongwei Feng
Yuting Feng
Tianxiang Gao

Chapter 1: Introduction

Global climate change is a major concern as affected by increasing CO_2 concentrations in the atmosphere (Canadella and Raupacha 2007, Fung 2013, Change 2007). One of the many ways discussed to mitigate these increasing CO_2 levels is to sequester some of that carbon from the atmosphere (Lin and Zhang 2012, Rice 2006). This is commonly done by growth of vegetation, thus monitoring plant productivity is a great way of estimating rates of carbon sequestration by that pool. A significant player in carbon sequestration by plants occurs within forests (Change 2007, Davis et al. 2009, Wang et al. 2012, Dixon et al. 1994, Fang et al. 2001), so being able to estimate forest productivity can help us better understand the global carbon cycle and identify solutions to enhancing carbon sequestration.

Plant growth, or the increase in its biomass, is commonly referred to as Net Primary Productivity (NPP) which is defined as the difference between photosynthesis and autotrophic respiration by vegetation per unit time and area (Lieth 1975). As an important component of the terrestrial carbon cycle, realizing the trend and variation of NPP can facilitate our understanding regarding the impact of past, present, and future climate change on terrestrial carbon sequestration across a range of spatial and temporal scales (Gmur et al. 2014, Vogt et al. 1996, Vogt et al. 2016, Gmur et al. 2012, Landres, Morgan and Swanson 1999). Invaluable information can be gained by retrieving historical data of NPP trajectories, which acts as a significant indicator of forest health condition, stand structure and disturbances (Wang et al. 2018, Birdsey, Pregitzer and Lucier 2006, Zhang et al. 2012). Since ground truthing measurement of annual NPP, with broad spatial coverage, is time-consuming and labor-intensive (Liu et al. 2002), remote sensing technology

combined with computer models could supplement and in some cases substitute for the traditional field-based approach to NPP quantification.

Three types of models have generally been used for NPP simulation (Ruimy, Saugier and Dedieu 1994) including statistical models (Lieth 1975, Zaks et al. 2007), parametric models (Potter et al. 2013, Potter, Klooster and Matson 1993) and process-based models (Running and Zhao 2015, Robinson et al. 2018, Liu et al. 1997, Liu et al. 2002). Statistical models were built upon the relationship between annual NPP and meteorological data (e.g., annual temperature, precipitation, evapotranspiration) through regression analysis (Liu et al. 1997, Zaks et al. 2007). Parametric models incorporated the "efficiency" concept to calculate the NPP, using parameters that include incident solar radiation, and light-use efficiency (LUE). Process-based models simulate the physiological process impacting the vegetation carbon uptake such as photosynthesis and autotrophic respiration. As a powerful tool revealing the mechanisms of vegetation carbon production and for exploring the feedback of ecosystem to the changing climate, the process-based models were assessed to be more reliable than other types of models for NPP simulation, due to its solid foundation on ecological processes (Liu et al. 1997).

Investigating the long-term variability of vegetation NPP could further our understanding regarding the influence of climate change on the dynamics of carbon exchange between terrestrial ecosystem and the atmosphere. Many studies have been undertaken to explore the spatial-temporal dynamics of NPP (Yang and Yu 2017, Liang et al. 2015) using a wide range of datasets and simulation models. However, huge uncertainties, in terms of the magnitude and trend, were observed when using different models and at various spatial scales (Wang et al.

2017). Therefore, a partnership between spatial and field-based information could provide us insight regarding the response of NPP to the climate and terrestrial conditions (Vogt et al. 2010). In addition to exploring the time-series NPP trajectories, it is important to understand the potential driving forces causing this spatial-temporal NPP variability, because this knowledge could help us to project the trend and magnitude of NPP in the future.

Previous studies suggested that the vegetation productivity was greatly affected by efficiency of using absorbed photosynthetic active radiation (APAR) (Gitelson et al. 2015, Potter et al. 1993). Therefore, the metrics (e.g., APAR, LUE) depicting the magnitude of radiation energy absorbed by vegetation for carbon production were widely used as an input to the process-based models and parametric models for NPP simulation. For example, The Moderate Resolution Imaging Spectroradiometer (MODIS) NPP dataset applied the MODIS Fraction of Photosynthetic Active Radiation (FPAR) data as an input parameter for NPP calculation (Running and Zhao 2015). Since the spatial resolution of the MODIS FPAR dataset is relatively coarse (500m*500m), an updated NPP product incorporated FPAR data with higher spatial resolution (30m*30m) which was constructed by using the empirical relationship with the Landsat Surface Reflectance (SR) dataset (Robinson et al. 2018). In order to precisely assess the impact of radiation energy on vegetation NPP variability, it is critical to use a high-resolution incoming solar radiation dataset that could describe the spatial pattern of incident radiation energy at very fine spatial scales. Previous studies showed that the topographic effect, including variations in slope and aspect, was the dominant factor causing the spatial variability in solar radiation at a regional scale (Dubayah and Loechel 1997, Pons and Ninyerola 2008). With the availability of the Airborne Light Detection and Ranging (LiDAR) system, we are able delineate the topographic information

based on the spatial distribution of LiDAR point cloud and quantify the incoming radiation energy, thus understanding its link to vegetation NPP variability at the regional scale.

Recent studies have provided the evidence that the changing climate has a strong influence on vegetation NPP variability (Schuur 2003, Lieth 1975, Zaks et al. 2007). However, the variation in NPP can also result from the indirect influence of climate through forest stand age, aboveground biomass and plant phenology (Michaletz et al. 2014). From a long temporal scale, the net carbon accumulation of the forest ecosystem heavily relies on the stand age, which is determined by the magnitude and frequency of forest disturbances (Chapin 2002, Kashian et al. 2006, Moskal and Jakubauskas 2013). Former research even suggested that the forest stand age could explain more variation in vegetation NPP compared with other climate variables, such as annual mean temperature and precipitation (Michaletz et al. 2014). Therefore, a comprehensive knowledge of the NPP-age relationship could improve our understanding regarding the carbon storage and flux dynamics across multiple scales and help us to project the impact of future disturbances on terrestrial carbon balance. In the past decades, some process-based biogeochemical models have been built to reflect both the disturbance and non-disturbance factors on the terrestrial carbon budget (Chen et al. 2000b, Chen, Chen and Cihlar 2000a). Those models were applied in many regions all over the world to investigate the NPP- stand age relationship among different forest types (Wang et al. 2018, Wang et al. 2011). However, the forest stand age map used in previous studies for model calibration is from the forest inventory dataset. Due to the availability of the field plot data, there are relatively huge uncertainties existing in forest age maps generated by inventory datasets. In order to overcome this shortage, an improved forest age mapping approach, relying on multi-temporal remote sensing data and

Vegetation Change Tracker (VCT) algorithm will be applied in this study to investigate the relationship between stand age and NPP among different forest types.

The Olympic Peninsula in the State of Washington has one of the largest temperate rainforests in the Unites States (Nadkarni 1984, Lomolino and Perault 2007). Temperate rainforests are among the world's biggest carbon sink, playing a critical role in terrestrial carbon cycle (DellaSala 2011, Sebastiaan et al. 2008, Smithwick et al. 2002, Keith, Mackey and Lindenmayer 2009) and climate regulation (Smithwick et al. 2002, Sebastiaan et al. 2008). Observing the long-term trends and variations of NPP in temperate rainforest could further our understanding on the vulnerability of temperate rainforest to our changing climate. This information will help us to better understand and even predict the terrestrial carbon cycle dynamics under climate changes.

The overall goal of this study is to investigate the impact of climate change and topography on carbon sequestration rates of temperate rainforest in our study area. The objectives include: 1) quantifying, validating and comparing the annual NPP in our two watersheds (Hoh and Queets) from 1986 to 2017 using different models, 2) investigating the direct (e.g., temperature, precipitation) and indirect effects (e.g., forest stand age) of climate change on NPP variability, and 3) mapping the LiDAR-based topographic solar radiation and exploring its relationship with vegetation NPP among different forest types.

Chapter 2: Materials and Methods

2.1 Study Area:

The study areas selected are located on the Olympic Peninsula of Washington State. We focused on two watershed regions, Queets and Hoh, as shown in Figure 2.1. Queets, the first watershed (Queets) is located in the Southeastern part of the peninsula with dominant species including *Tsuga heterophylla* and *Picea sitchensis*. Hoh, the second watershed (Hoh) is situated on the Midwestern part of the peninsula and the forest cover is dominated by *Acer circinatum*, and *Rubus spectabilis*. Generally, the Olympic Peninsula has a temperate maritime climate with warm summers and cool winters (Lewis et al. 2016, Peel, Finlayson and McMahon 2007). The topography on the peninsula is very complex with forest being the dominate land-cover type (Schwörer et al. 2016). There is a prominent topographic influence caused by the Olympic mountains regarding the precipitation patterns across the peninsula. The western slopes, with higher elevations, receive over 5000 mm of annual precipitation while the locations in the rain shadow region to the northeast and on the other side of the Olympic Mountains receive less than 500 mm of annual precipitation (Schwörer et al. 2016). This steep precipitation difference, combined with the differing temperatures, produce a variety of climatic conditions across the peninsula. Due to the drier climate in the eastern and northeastern areas of the peninsula, wildfires in those regions play an important role in forest disturbance and regrowth (Henderson and United States. Forest Service. Pacific Northwest 1989). Therefore, these wildfires are an influencing factor on the aboveground NPP variability.

a. Geographical Location

b. Hoh

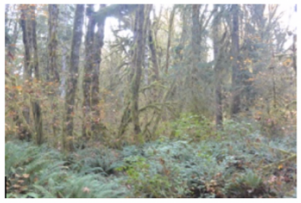

c. Queets

Figure 2.1: (a) The geographical locations of the two watersheds. (b and c) The forest structure and species composition in Queets (watershed#1) and Hoh (watershed#2).

2.2 Field Data:

Ground-truthing data plays an important role in model validation. In this study, we used annual aboveground NPP data from the North America Carbon Program, Terrestrial Ecosystem Research and Regional Analysis- Pacific Northwest (NACP TERRA-PNW) (Law and Berner 2015) to evaluate the model performance by comparing the field-based NPP with the model-derived NPP. The field data were collected across forests in Washington, Oregon and California by the TERRA-PNW research group between 1999 and 2014.

Each sample plot consists of a 1-ha area with four subplots for each (center, north, southwest, southeast). Starting at the subplot center, and taking into consideration the tree density, each subplot was spaced at 35m, with the subplot diameter ranging from 10m to 17m (Law and Berner 2015). The plot-level NPP was estimated based on the difference in biomass at two points in time, divided by the number of intervening years between data collection.

2.3 Climatic Data:

The annual mean temperature and precipitation data from 1986 to 2017 in Queets plot and Hoh plot were retrieved from the Parameter-elevation Relationships on Independent Slopes Model (PRISM) group in order to facilitate our understanding of how the changing climate contributes to the annual NPP variation. The historical temperature and precipitation data were estimated using PRISM, considering the climate-elevation regression for each grid cell of the digital elevation model (DEM) (Daly et al. 2008). In order to quantify the annual NPP in each of the sample plots we used statistical models with climatic data input. We also retrieved the annual mean precipitation and temperature data at specific years when the ground-truthing NPP was estimated.

2.4 Remote Sensing Data:

2.4.1 Landsat Data:

Geometrically and radiometrically corrected Landsat 8 Operational Land Imager (OLI) data acquired in 2010, with 30m spatial resolution, were obtained from the U.S. Geological Survey/ Earth Resources Observation and Science (USGS/EROS) Landsat archive. In order to obtain the best quality data, imagery with the lowest cloud% was selected during the peak growing season to minimize the sun angle differences, vegetation phenology effect and other exogenous factors (Wenjuan et al. 2016). The Landsat 8 OLI imagery was atmospherically calibrated to surface reflectance by using the Landsat Ecosystem Disturbance Adaptive Processing System (LEDAPS) algorithm (Masek et al. 2006) and the Landsat 8 surface reflectance code (laSRC) (James et al. 2017). Individual bands, spectral indices and first principal components were extracted from Landsat 8 imagery to test their sensitivity to the forest NPP variability across our study region.

All the selected variables extracted from the Landsat surface reflectance data are illustrated in Table 1.

Table 1: Variables selected to test their sensitivity to the NPP variability in two watersheds (Queets and Hoh).

Variables	Formula	Reference	Description
G, R, NIR			Landsat 8 bands
MSAVI	MSAVI=(2*Band4+1-sqrt((s*Band4+1)^2-8*(Band5-Band4))	(Qi et al. 1994)	Modified Soil-adjusted Vegetation Index
EVI	EVI=2.5*((Band5-Band4)/(Band5+6*Band4-7.5*Band2+1))	(Huete et al. 2002)	Enhanced Vegetation Index
NDMI	NDMI=(Band5-Band6)/(Band5+Band6)	(Gao 1996)	Normalized Difference Moisture Index
NDVI	NDVI=(Band5-Band4)/(Band5+Band4)	(Rouse 1973)	Normalized Difference Vegetation Index
SAVI	SAVI=((Band5-Band4)/(Band5+Band4+0.5))*1.5	(Huete 1988)	Soil-adjusted Vegetation Index
PCA1			First Principal Component

2.4.2 Land-cover data:

Land-cover is considered as one of the significant drivers of environmental productivity (Mildrexler et al. 2007). So land-cover data were obtained in this study to investigate the impact of changing climate and topography on NPP variations in different forest types. We extracted the land-cover information from the National Land Cover Database (NLCD), which provides land-cover data across the United States at 30m spatial resolution with a 16-class legend based on a modified Anderson Level II classification system (Yang et al. 2018, Homer et al. 2015). In order to evaluate the NPP differences among different forest types in the two watersheds (Queets and Hoh), we extracted three forest classes (deciduous forest, evergreen forest and mixed forest) from the NLCD and calculated the annual mean NPP value of each forest class in our study region during the period from 1986 to 2017. Percent tree canopy data within our two watersheds were also derived from NLCD with a 30m spatial resolution (Coulston et al. 2012, Coulston et al. 2013) to test the impact of forest cover percentage on regional NPP variability. The land-

cover types and forest cover percentage in the two watersheds of Hoh and Queets are illustrated in Figure 2.2.

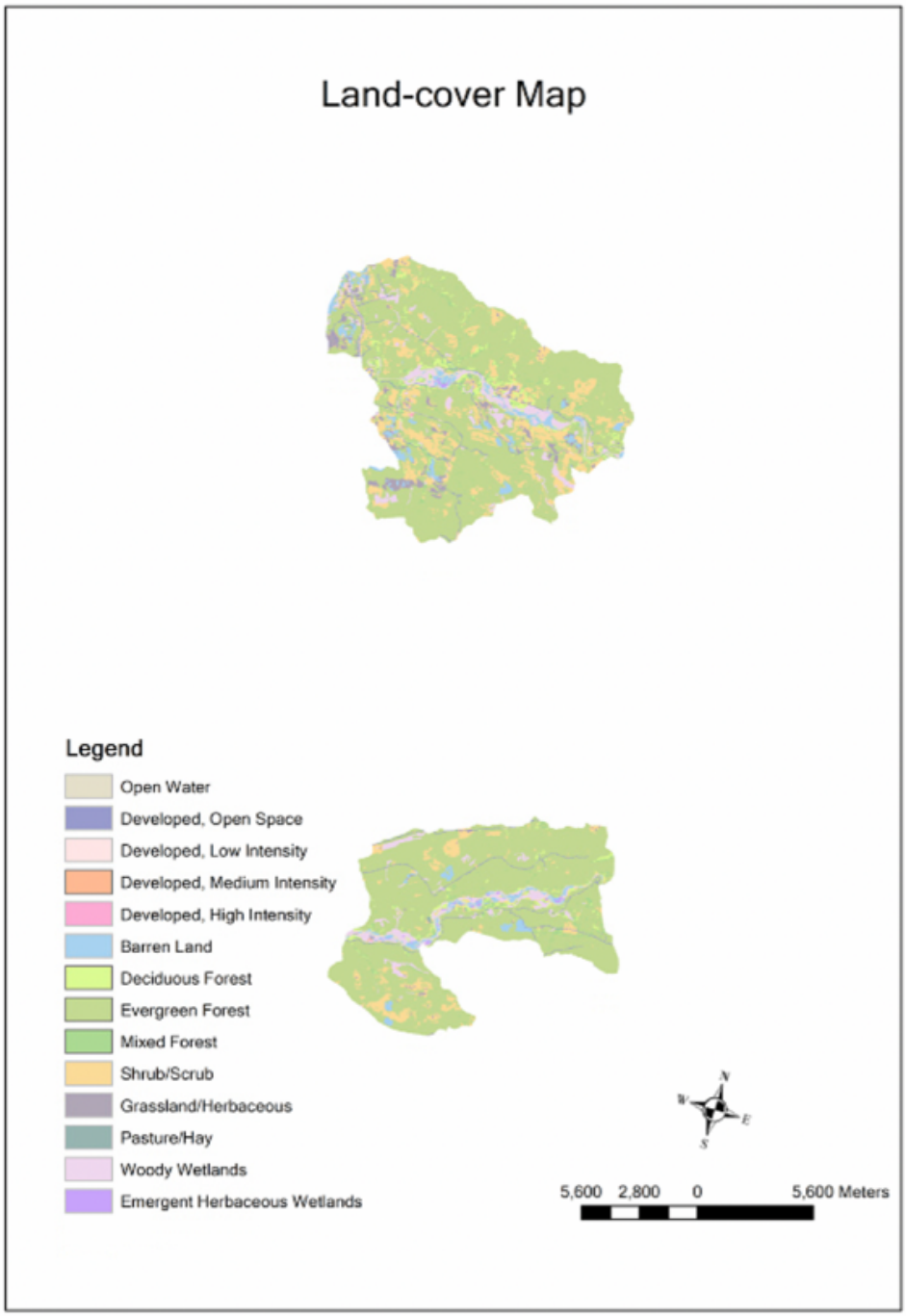

a. Land-cover Map

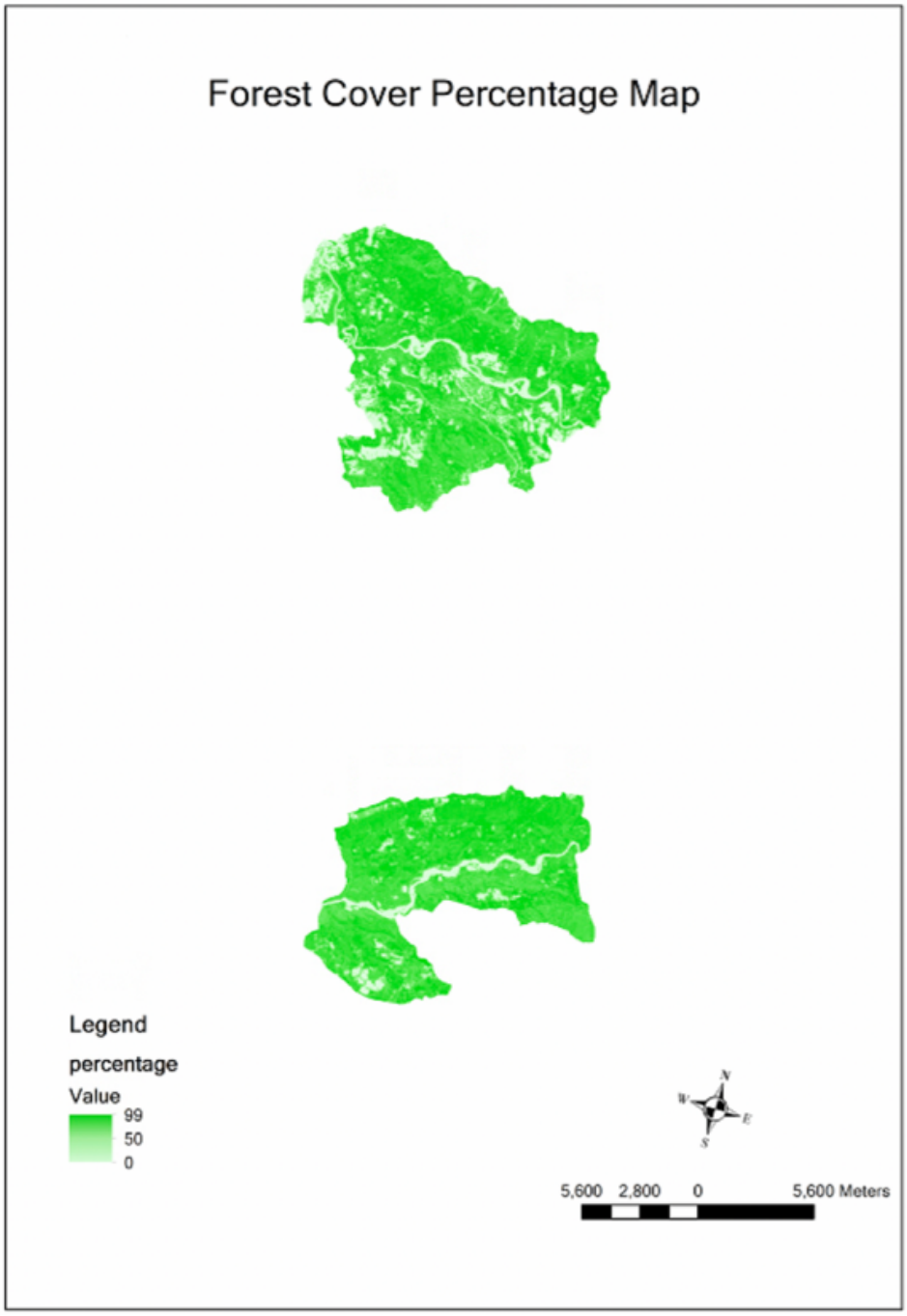

b. Forest Cover Percentage Map

Figure 2.2: (a) Land-cover pattern of our study area; (b) Forest Cover Percentage distribution in two watersheds (Queets and Hoh).

2.4.3 MODIS LAI Data:

In order to assess the influence of canopy vertical structure on NPP variations across Queets plot and Hoh plot, Leaf Area Index (LAI) data covering the two watersheds were obtained in this study from the MODIS Collection 6 LAI/FPAR product generated at a spatial resolution of 500m and with an 8-day temporal resolution (Myneni, Knyazikhin and Park 2015).

Due to the huge data volume, we used the Google Earth Engine to derive the time-series LAI trajectories in both Queets plot and Hoh plot from 2002 to the present day and calculated the mean annual LAI values, respectively. LAI trajectories in our two watersheds from 2002 to 2017 are presented in Figure 2.3.

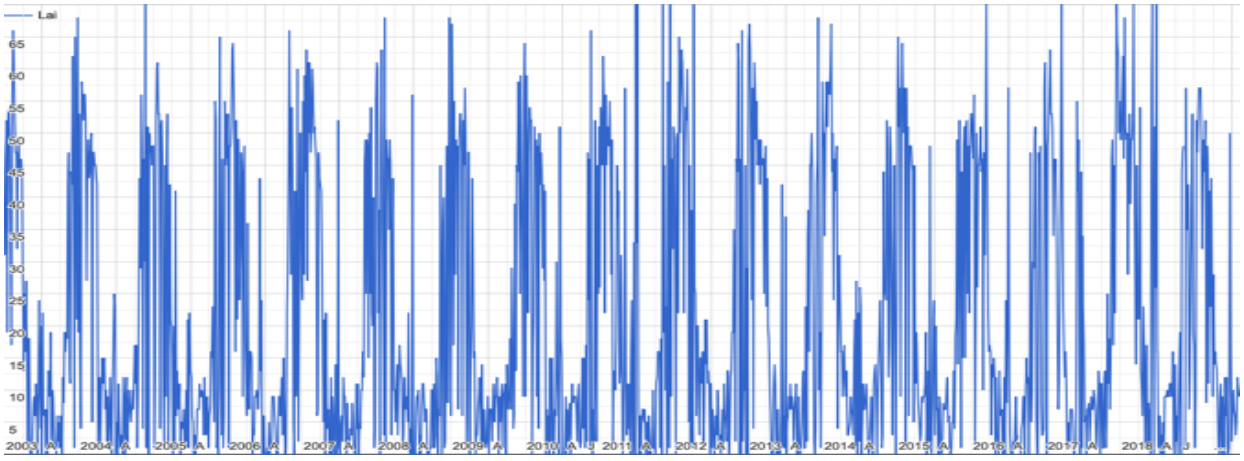

a. Time-series LAI trajectories in Queets plot.

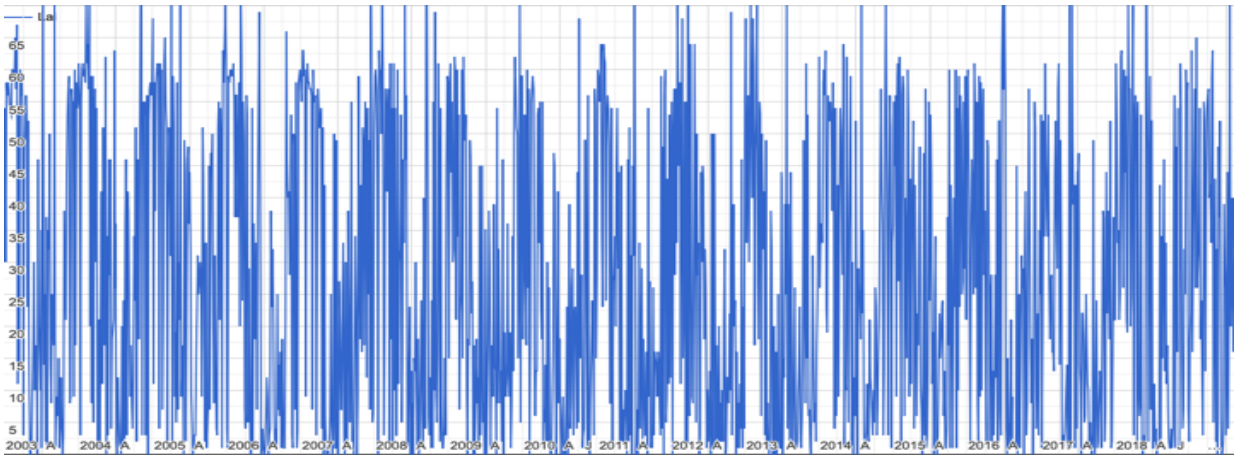

b. Time-series LAI trajectories in Hoh plot.

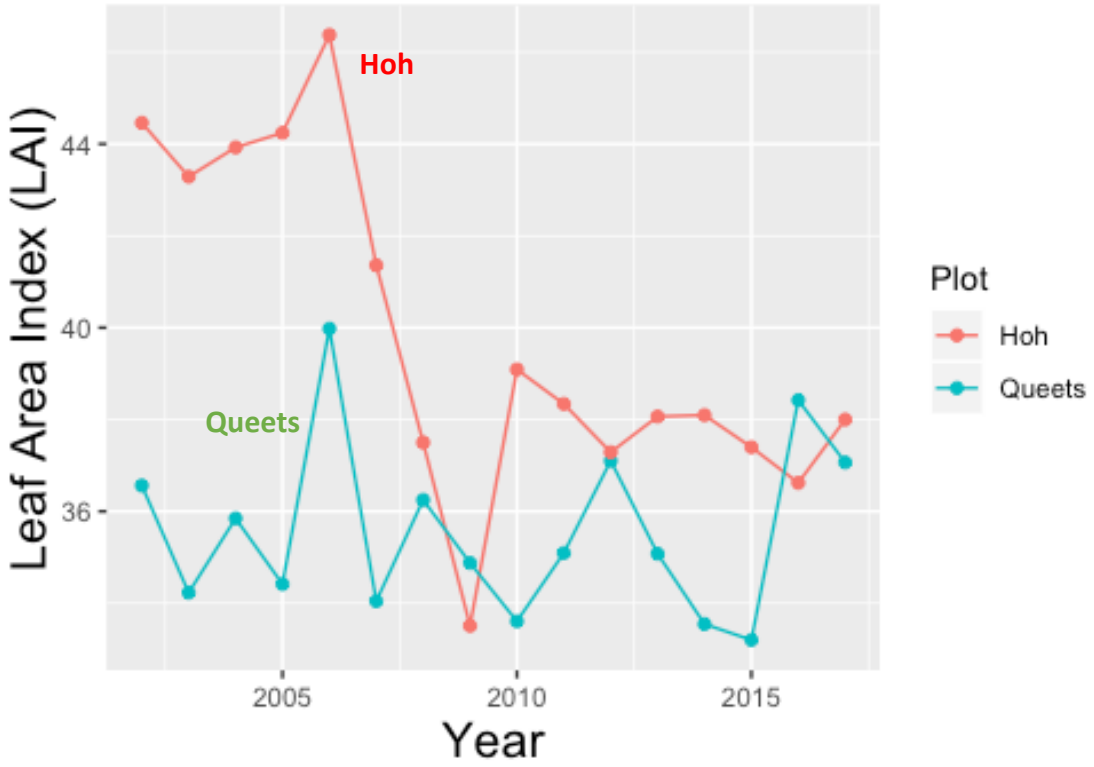

c. Annual mean LAI in Queets plot and Hoh plot from 2002 to 2017.

Figure 2.3: (a, b) The time-series LAI trajectories in Queets plot and Hoh plot respectively and (c) the annual mean LAI variation in the Queets plot and Hoh plot from 2002 to 2017.

2.4.4 National Digital Elevation Model (DEM):

The DEM data used in our study region have a spatial resolution of 10m (Geological 1999). We extracted the data from the National Elevation Dataset developed by the USGS Earth Resources Observation and Science (EROS) Data Center (Gesch et al. 2002). In order to evaluate the effect of topography on regional NPP variability, we applied Topographic Solar Radiation Index (TSRI) to empirically estimate the difference of incident solar radiation due to the topographic effect. The TSRI was calculated based on the slope information derived from the DEM data (Ferguson, Johnson and Morgan) using the following equation:

$$TSRI = 1- \cos ((\ pi/180\ ) * (\ aspect- 30))/2 \quad (1)$$

The spatial patterns of TSRI derived from the DEM data are shown in Figure 2.4(a).

2.4.5 Airborne LiDAR Data:

The airborne LiDAR data over the research plots were acquired in April 16th, 29th , 30th , May 1st , November 6th -19th and December 1st – 4th , 2011 with Leica ALS50 Phase II and ALS60 system, respectively. The average point density is ≥ 8 pulses per square meter over the terrestrial surface. The datasets including Point Cloud, Digital Terrain Model (DTM) and Digital Surface Model (DSM) were obtained from the Washington State Department of Natural Resources (DNR) LiDAR Portal. The LiDAR-based DTM and DSM have higher spatial resolution (1 meter) when compared to the DEM extracted from the National Elevation Dataset. The spatial patterns of TSRI in Queets plot and Hoh plot calculated by slope information derived from DTM data are depicted Figure 2.4(b).

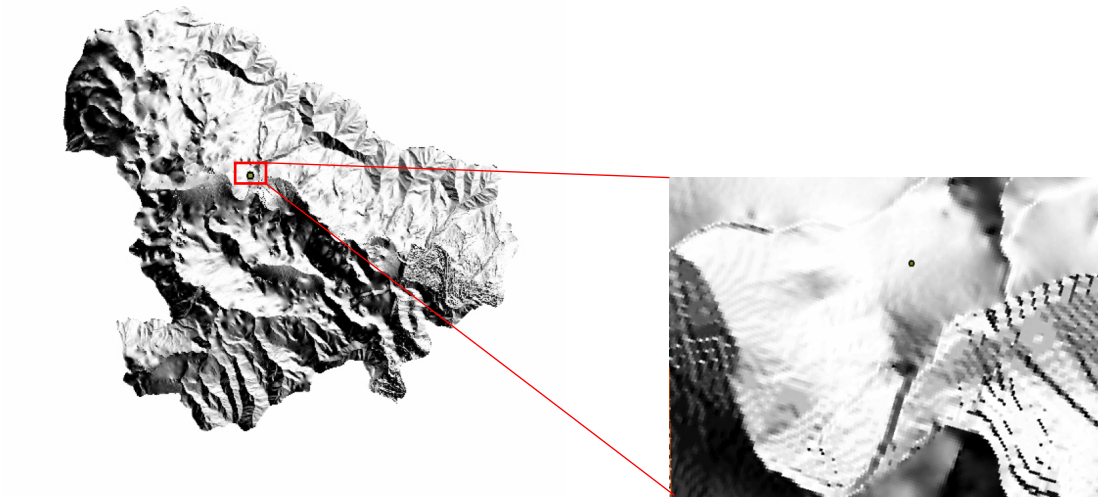

(a)

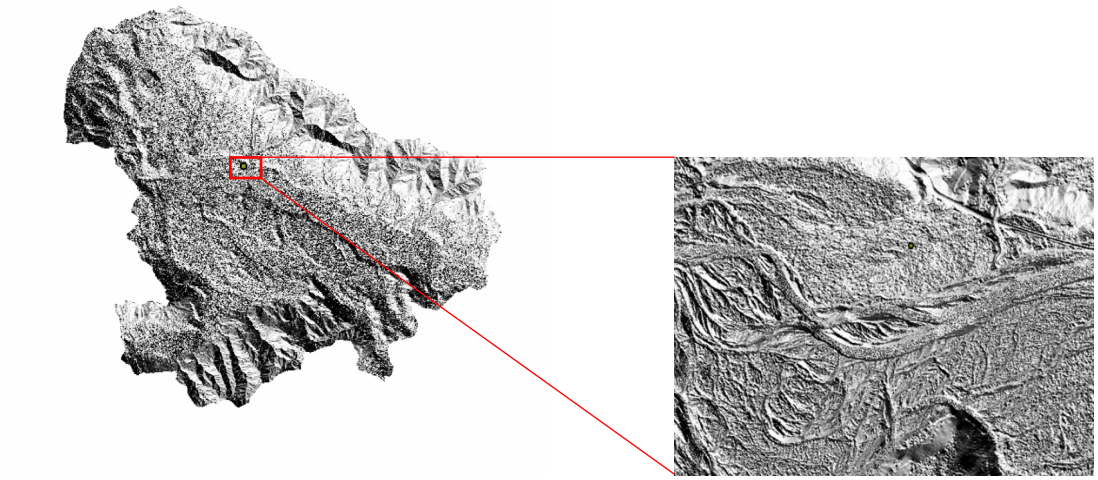

(b)

Figure 2.4: (a) The spatial pattern of TSRI derived from National DEM and (b) Airborne LiDAR.

We also derived the Rumple Index from LiDAR-based DSM and DTM in order to explain the NPP variability across the two plots. The Rumple Index was calculated as the ratio of canopy surface area to the ground surface area (Parker et al. 2004). The canopy surface grid points of

both plots were used to create the triangular irregular network (TIN) of the three-dimensional points, and then divided by the ground surface area (Kane et al. 2008).

2.5 NPP simulation Models:

2.5.1 Biome-BGC Model:

Landsat-derived annual NPP data for the conterminous United States, with 30 meters spatial resolution, spanning the years from 1986 to 2017 were used in this study. The NPP data was simulated using the Biome-BGC model with input variables including vapor pressure deficit (VPD), incident shortwave radiation (SWrad), average daytime temperature (Tavg), daily minimum temperature (Tmin), land-cover data, fraction of photosynthetically active radiation (FPAR) and leaf area index (LAI) (Robinson et al. 2018). The logic used in calculating the annual NPP is demonstrated in Figure 2.5. The annual mean NPP of two plots and two watersheds were extracted from the Google Earth Engine platform and further statistical analyses was conducted in R.

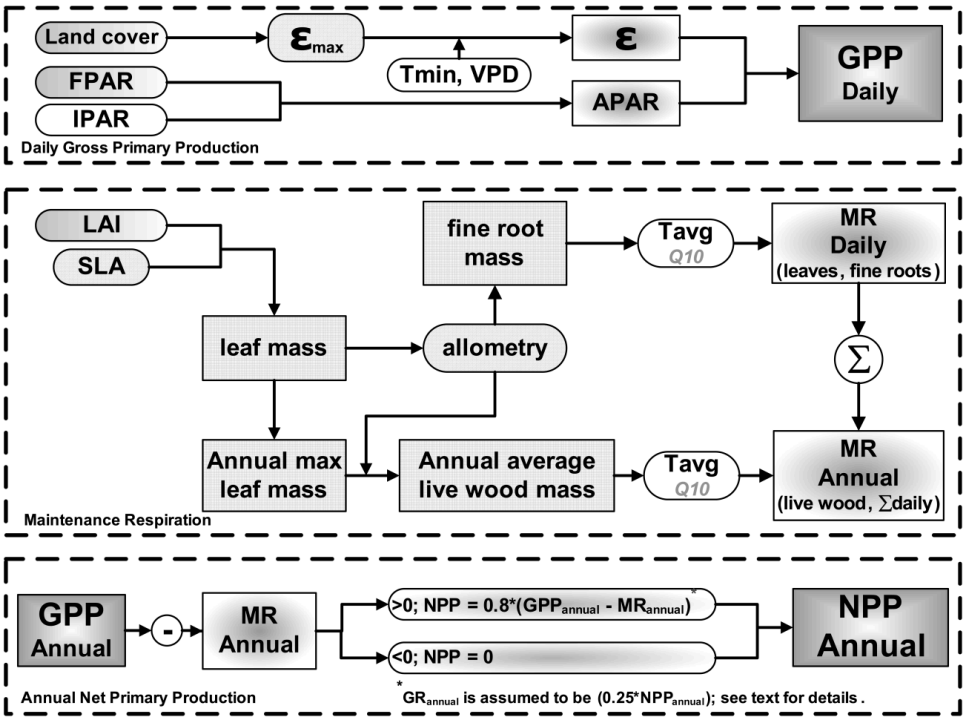

Figure 2.5: Flowchart describing the steps calculating the 8-day GPP and annual NPP (Running and Zhao 2015).

The MODIS NPP data (MOD17) was also applied in this study to test the influence of the spatial resolution of input variables on NPP simulation accuracy. Compared with the Landsat derived annual NPP data, MOD17 applied the same process-based model (Biome-BGC) for annual NPP simulation with input variables of coarser spatial resolution (Robinson et al. 2018). In order to keep the data consistent for further field- and cross-validation, MODIS annual NPP data from 2004 to 2013 was obtained for use in this study.

2.5.2 Carnegie Ames Stanford Approach:

The Carnegie Ames Stanford Approach (CASA) model has been widely used for forest NPP quantification and assessment across different spatial scales (Hao et al. 2018, Mu et al. 2013, Wen, Liu and Du 2018). We obtained the global-scale terrestrial NPP data provided by NASA

Ames Research Center, with 8 km spatial resolution for the years from 2004 to 2013 (Potter et al. 2013). The annual predicted NPP values of each sample plot (Queets and Hoh) was extracted from the CASA NPP product for the cross-validation.

2.5.3 Thornthwaite Memorial Model:

Based on temperature and precipitation data, to quantify the forest annual NPP, the Thornthwaite Memorial model was applied in this study. This model provides an empirical relationship between forest NPP and different climatic factors including precipitation, temperature and evapotranspiration (Lieth 1975). Compared with the process-based models, this statistical model is easy to operate with only a few parameters required, and has a higher spatial and temporal resolution (Yang and Yu 2017). The following equations expressed the procedures of calculating the forest NPP:

$$NPP = 3000 * (1-e^{-0.0009695 * |v-20|}) \quad (2)$$

$$v = \frac{1.05*R}{\sqrt{1+(1+1.05\frac{R}{L})^2}} \quad (3)$$

$$L = 3000+25 * T +25T^3 \quad (4)$$

T: annual mean temperature (°C); R: annual mean precipitation (mm); L: annual mean evapotranspiration (mm); V: annual mean actual evapotranspiration (mm).

2.5.4 Miami Model:

Considering the meteorological factors (Zhou et al. 2015), we used the Miami Model to estimate the annual NPP. As the first global vegetation model developed for NPP quantification, the Miami Model has been used worldwide and also acts as a baseline for model comparisons (Hao

et al. 2018, Yang and Yu 2017, Adams, White and Lenton 2004). This model empirically correlates annual mean temperature and precipitation with NPP. The formula of this model is shown below:

$$\text{NPP} = \min\ \{(\frac{3000}{1+\exp\ (1.315-0.119t)}), (3000[1-\exp(-0.000664r)])\} \quad (5)$$

t: annual mean temperature (°C); r: annual mean precipitation (mm)

The annual mean temperature and precipitation data used as input for the Thornthwaite Memorial Model and Miami Model were derived from the data described in Section 2.3.

2.6 Forest Stand Age:

In this study, we acquired the forest disturbance and regrowth data developed by the North American Forest Dynamics (NAFD) projects (Goward et al. 2012, Goward et al. 2008). The NAFD dataset provides the forest disturbance and regeneration data from 1984 to 2010 for 55 sites across the conterminous United States and was produced by using the Landsat time-series stacks and the Vegetation Change Tracker (VCT) algorithm (Huang et al. 2009). The forest disturbance history of our study region (p48/r27) were extracted from the NAFD dataset. The VCT algorithm provides the disturbance product, where each pixel was labeled as one of the four categories including persistent non-forest, persistent forest, persistent water or with the year of change for disturbed forest pixels (Huang et al. 2010). The forest age was calculated as the difference between the year of disturbance and the year when the last Landsat scene was collected. Due to the time span of the Landsat stacks, we excluded all the pixels labeled as persistent non-forest, persistent forest and persistent water. Therefore, only forest pixels with disturbance history were used for stand-age calculation. The forest disturbance and stand age map for our study region are presented in Figure 2.6.

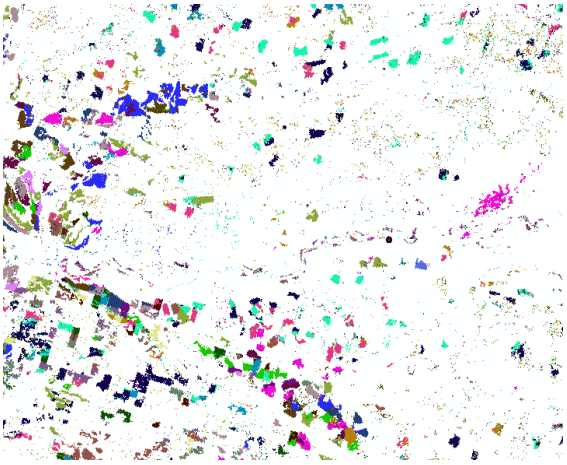

a. Forest disturbance map

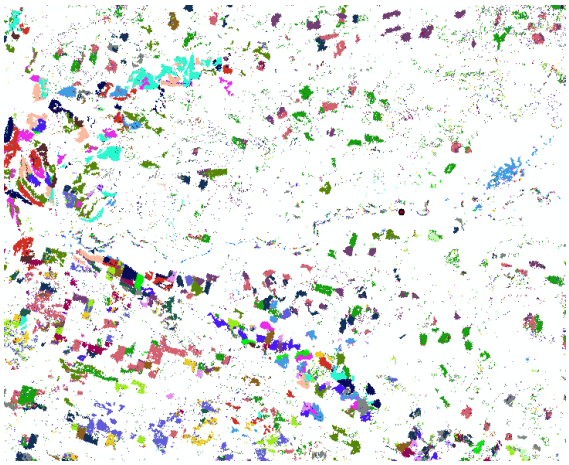

b. Stand age map

Figure 2.6: (a) The forest disturbance map, and (b) Forest stand age map derived from time-series Landsat data coupled with the VCT algorithm.

2.7 Trend Analysis and Turning Points Detection:

We used the Theil-Sen median slope estimator to assess the rate of change of annual NPP from 1986 to 2017. This approach is capable of helping us evaluate the rate of change of the time-series data with short time span and noise interference (Zhou et al. 2016). The Theil-Sen median estimator was calculated as:

$$\beta_i = \text{Median}\left(\frac{x_j - x_k}{j-k}\right) \text{ for } i=1,\ldots\ldots,N \qquad (6)$$

Where x_j and x_k represents the NPP value for year j and k (j>k).

After observing the general trend of the time-series NPP trajectory, we then applied the piecewise linear regression (PLR) approach to detect the time and magnitude of potential changes in NPP trajectory (Toms and Lesperance 2003). This model has been widely used in ecological research to detect the potential Turning Points (TP) in noisy time-series data (Liang et al. 2015, Peng et al. 2011). Two factors are carefully considered when visually estimating the potential TP in the trajectory: 1) short segments before or after the potential TP should be

avoided (Xu et al. 2014), and 2) the maximum number of potential TP should be specified in advance so as to avoid the complex results and uncertainty in understanding the trend of NPP trajectories (Wen et al. 2017). The PLR model was computed as:

$$\gamma = \begin{cases} \beta_1 * t + \beta_0 + \varepsilon & (t <= \alpha) \\ \beta_1 * t + \beta_2 + (t - \alpha) + \beta_0 + \varepsilon & (t > \alpha\ ) \end{cases} \quad (7)$$

γ: annual NPP; t: year; α: year of the TP; β_0: intercept; β_1: magnitude of the NPP trend before TP; $\beta_1+\beta_2$: the magnitude of the NPP trend after the TP; ε: residual.

The Akaike Information Criterion (AIC) was applied to determine the significance of the potential TP by fitting two models to the NPP trajectory (Akaike 1974, Yang and Yu 2017, Peng et al. 2011).

$$\text{AIC} = n * \log\left(\frac{RSS}{n}\right) + 2k + \frac{2k(k+1)}{n-k-1} \quad (8)$$

n: sample size; RSS: residual sum of square for the estimated model; k: number of parameters.

Finally, we calculated the ΔAIC, which was defined as the difference between the AIC_2 of the PLR model and the AIC_1 of the linear regression model. The threshold of ΔAIC was set to 2 and the potential TP was statistically significant when the ΔAIC was less than the defined threshold (Burnham 2002).

After retrieving the significant TP from the annual NPP trajectories, we then placed the same potential TP on both the annual temperature and precipitation trajectories from 1986 to 2017 in order to explore the impact of climate change on annual NPP variability. The same processes were followed as described above using both the PLC model and AIC models.

2.8 Validation:

Both the ground-truthing validation and cross validation approaches were used to assess the accuracy of the NPP estimation results simulated by statistical models and process-based models. The ground-truthing data we used can be found in Section 2.2.

Chapter 3: Results

3.1 Ground-truthing Validation and Cross Validation:

In this study, we used both process-based models and statistical models to predict annual NPP. In order to evaluate the accuracy of NPP simulation, we compared the field-based NPP with model-simulated NPP at the same geographic locations. Specifically, both Landsat-based and MODIS-based NPP data were applied to the Biome-BGC model for the simulation process. However, the spatial resolution of the input dataset differed. Therefore, the ground-truthing validation will help us to understand how different models and input data will influence the simulation accuracy. The results of ground-truthing validation were shown in Figure 3.1. In general, the annual NPP simulated by process-based models, including Biome-BGC and CASA, demonstrated a higher accuracy when compared with the NPP predicted by the statistical models. The quality of the input dataset also played an important role on precisely predicting the NPP variability. A stronger relationship between observed NPP and Landsat-based NPP was witnessed when compared with the NPP data simulated using the MODIS dataset with a coarser spatial resolution.

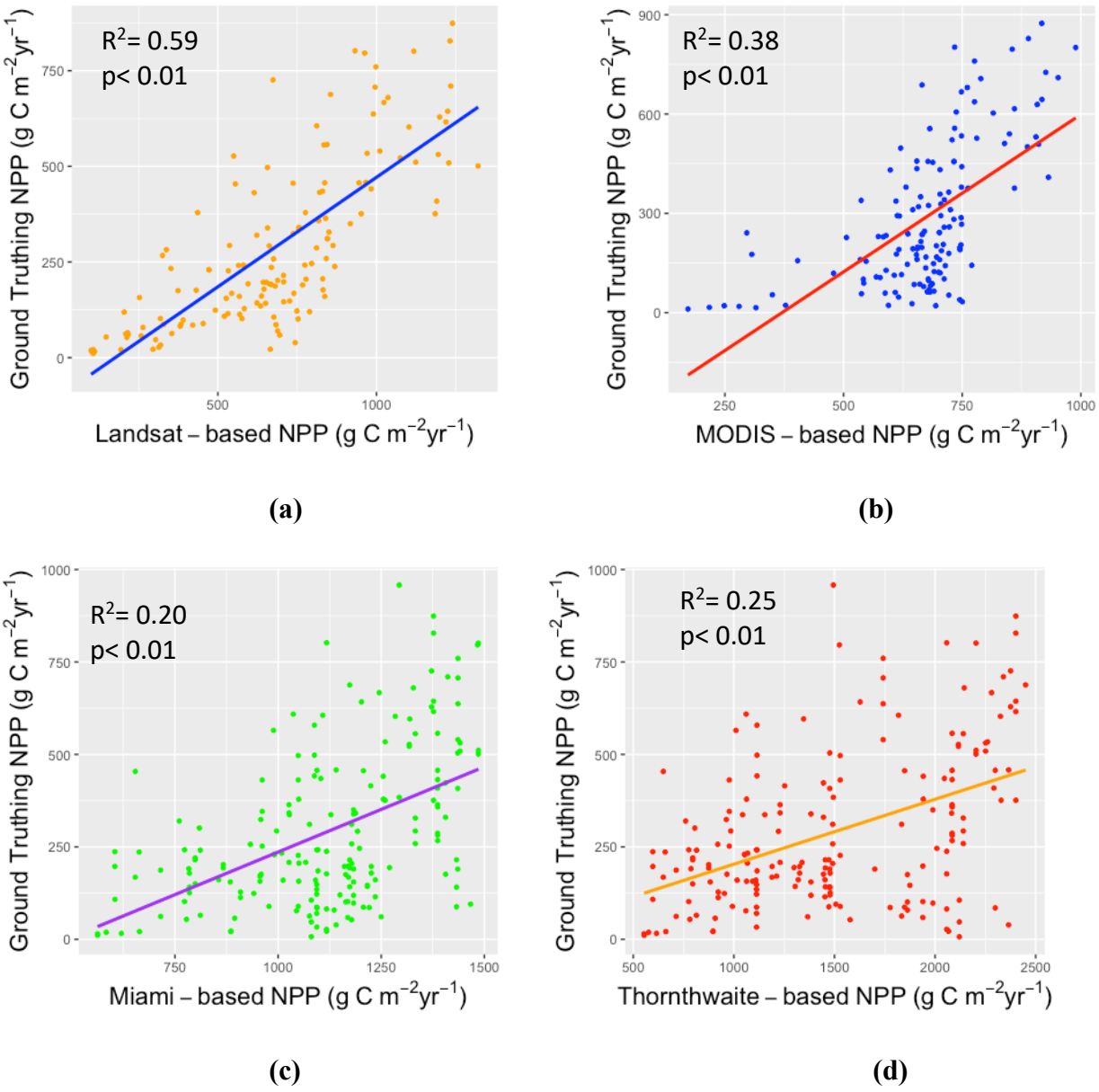

Figure 3.1: The relationship between field-based NPP and predicted NPP simulated by (a) Biome-BGC model with Landsat input, (b) Biome-BGC model with MODIS input, (c) Miami model and (d) Thornthwaite Memorial model.

To assess the relationship among NPP products simulated by different models and input datasets, cross-validation was applied in this study. Due to the data availability, the annual NPP values in our watershed region ranging from 2004 to 2013, were extracted from NPP datasets. The correlation matrix describing the relationship among different NPP datasets is shown in Figure

3.2. Positive relationships were observed among Landsat-based NPP, MODIS-based NPP, CASA NPP and Miami NPP datasets. Specifically, annual NPP product simulated by the Miami model demonstrated strong correlation with NPP datasets simulated by process-based models.

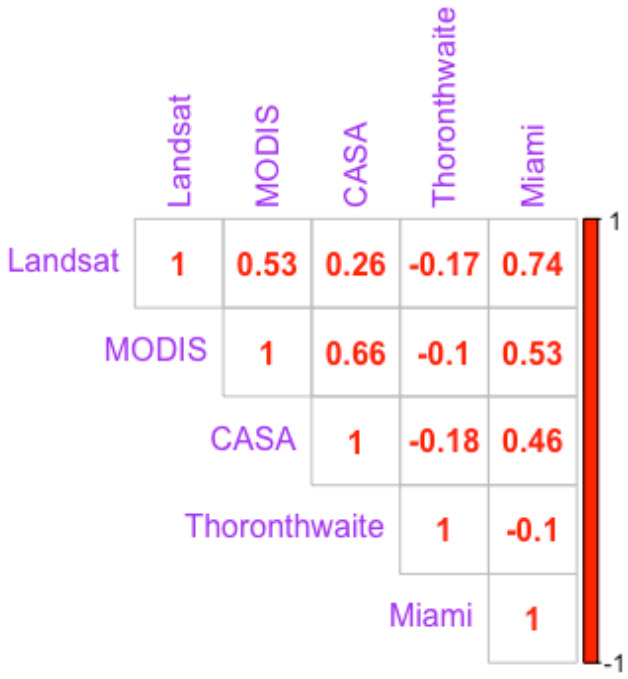

Figure 3.2: Pairwise correlation matrix depicting the relationship among NPP data using different models and input datasets.

3.2 NPP variation in two watersheds:

We retrieved the NPP trajectories of our two watersheds (Queets and Hoh) from 1986 to 2017 using the Google Earth Engine. The long-term NPP trajectories in our two plots are illustrated in Figure 3.3. The annual NPP in Hoh plot was higher than that in Queets plot. A One-way ANOVA test was then performed (Figure 3.4) and the results showed that the annual NPP in two plots were statistically different.

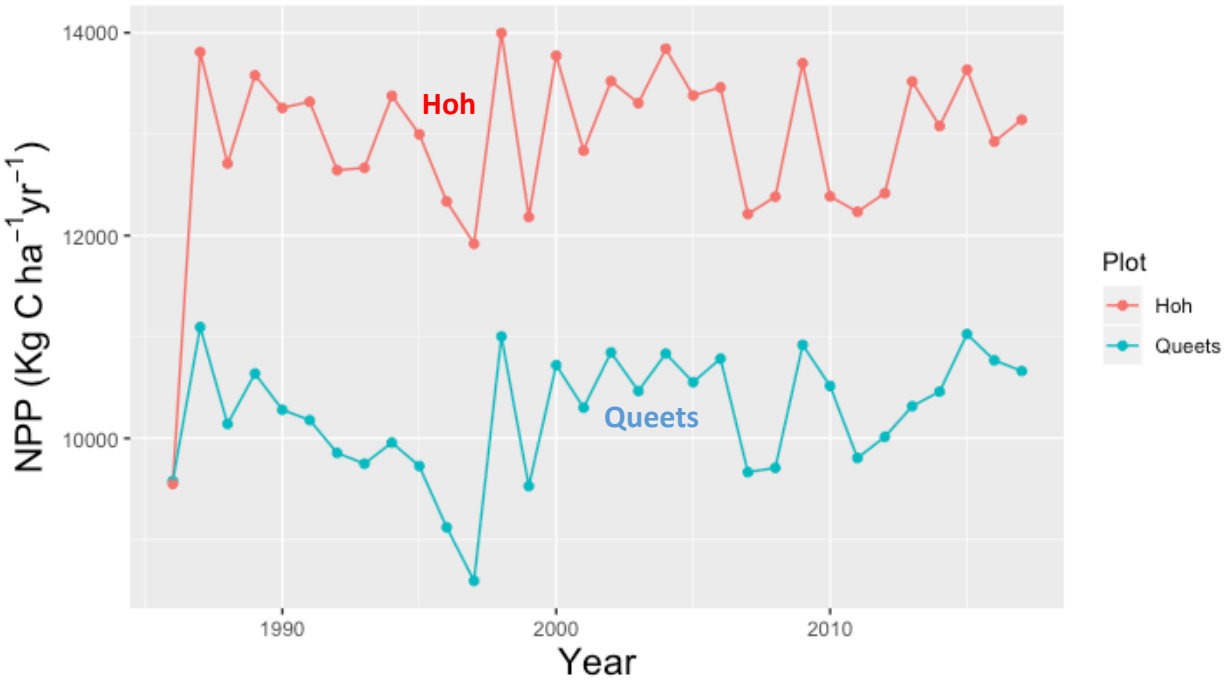

Figure 3.3: The time-series trajectories of the annual NPP in our two research plots (Queets plot and Hoh plot).

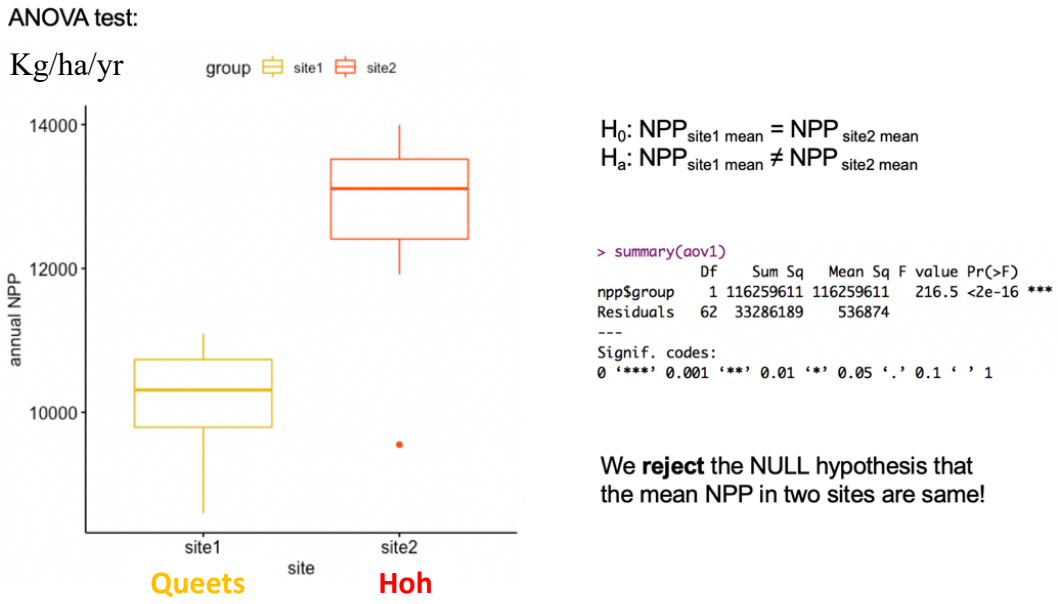

Figure 3.4: The results of a one-way ANOVA test comparing annual NPP between two watershed plots (Queets and Hoh).

3.3 Time-series Analysis:

To explore the general trend and Potential Turning Points, the Theil-Sen median slope estimator and Pairwise Linear Regression Approach discussed in Section 2.7 were applied to the long-term NPP trajectory in plot 1 (Queets). A general increasing trend was observed with two statistically significant turning points being detected in 1997 and 2007 (ΔAIC= 11.44). In order to explain the driving forces of the occurrence of the potential Turning Points, we placed the two turning points on the long-term annual temperature and precipitation trajectories ranging from1986 to 2017. The same turning points of 1997 and 2007 were found to be significantly different, regarding temperature trajectories. This indicates that the NPP was potentially influenced by temperature variability.

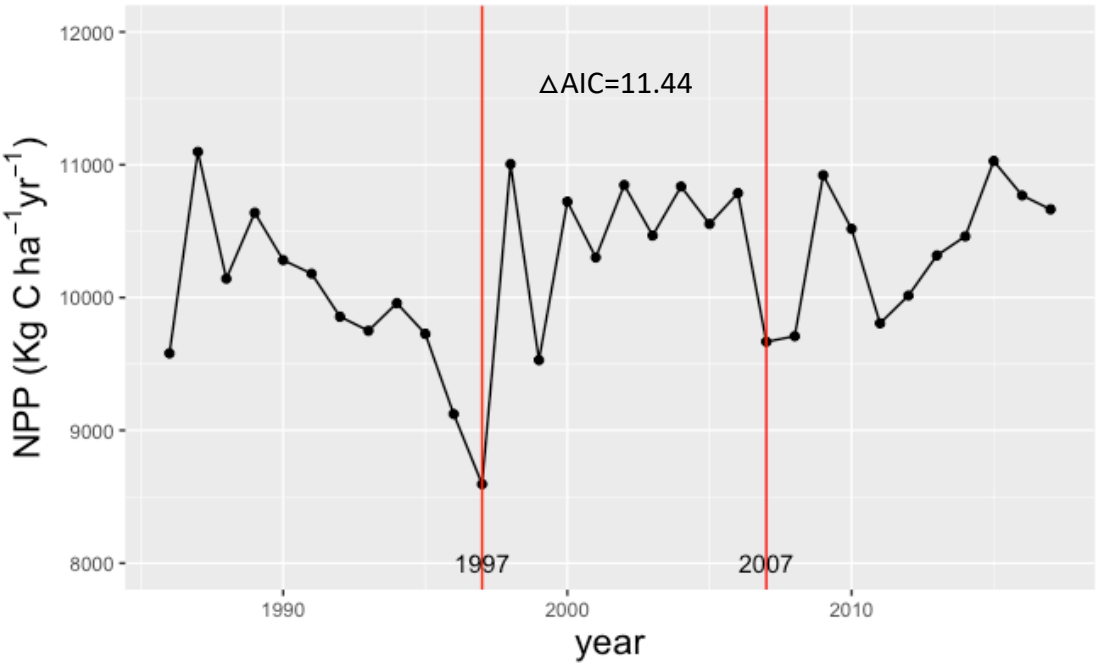

a. Potential Turning Points detected in annual NPP trajectories

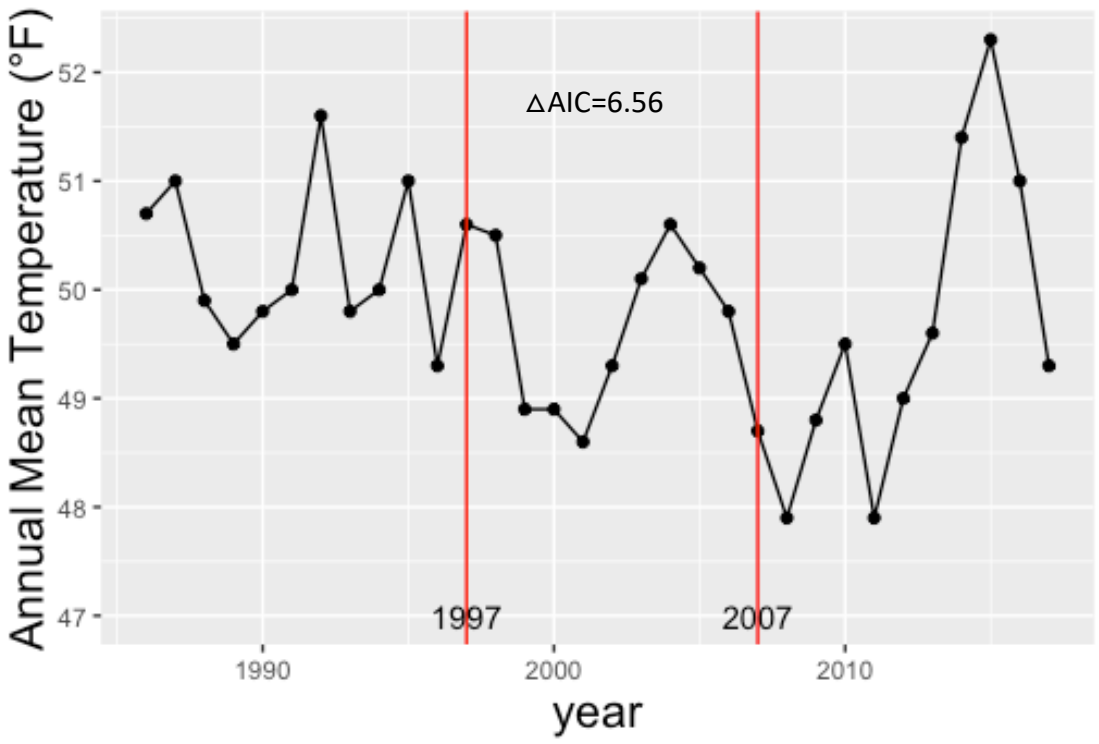

b. Potential Turning Points detected in annual temperature trajectories

Figure 3.5: Potential Turning Points detected in annual NPP trajectories (a) and annual temperature trajectories (b).

3.4 Influence of climate change on NPP:

The annual NPP data in Queets plot and Hoh plot from 2004 to 2013 were extracted from different NPP products. In order to analyze the impact of climate change on NPP variation, we then derived the annual mean precipitation and temperature during the same period in both research plots. Correlation analyses were conducted between NPP datasets and climate factors aiming to understand the sensitivity of different NPP products to the changing climate. Correlation coefficients between climate data and NPP values extracted from different NPP models are shown in Table 3.1.

Table 3.1: Correlation coefficient between climate data and different NPP dataset.

	Annual Mean Precipitation	Annual Mean Temperature
Landsat NPP (Biome-BGC)	-0.15	0.74
MODIS NPP (Biome-BGC)	-0.14	0.66
NPP (CASA)	-0.26	0.73
NPP (Miami model)	-0.14	
NPP (Thornthwaite Memorial model)		-0.12

The correlation coefficient between annual mean temperature and NPP derived from the Miami model was neglected because they are linearly correlated. Due to the same reason, we ignored the relationship between annual mean precipitation and NPP extracted from Thornthwaite Memorial model. The results showed that most of the models had a sensitive response to the changing annual mean temperature while the annual mean precipitation was not a dominant factor on NPP variability in our two research plots.

3.5 Impact of topography on NPP:

The TSRI derived from National DEM and LiDAR-based DTM was used to investigate the impact of solar radiation differences on regional NPP variability. We overlapped the TSRI maps with NLCD to delineate the TSRI patterns in each forest class (i.e., deciduous forest, evergreen forest, mixed forest). For each forest class, 24 sample points were randomly selected and correlated with the NPP. The relationships between NPP and TSRI derived from National DEM and LiDAR-based DTM for each forest type are illustrated in Figure 3.4.

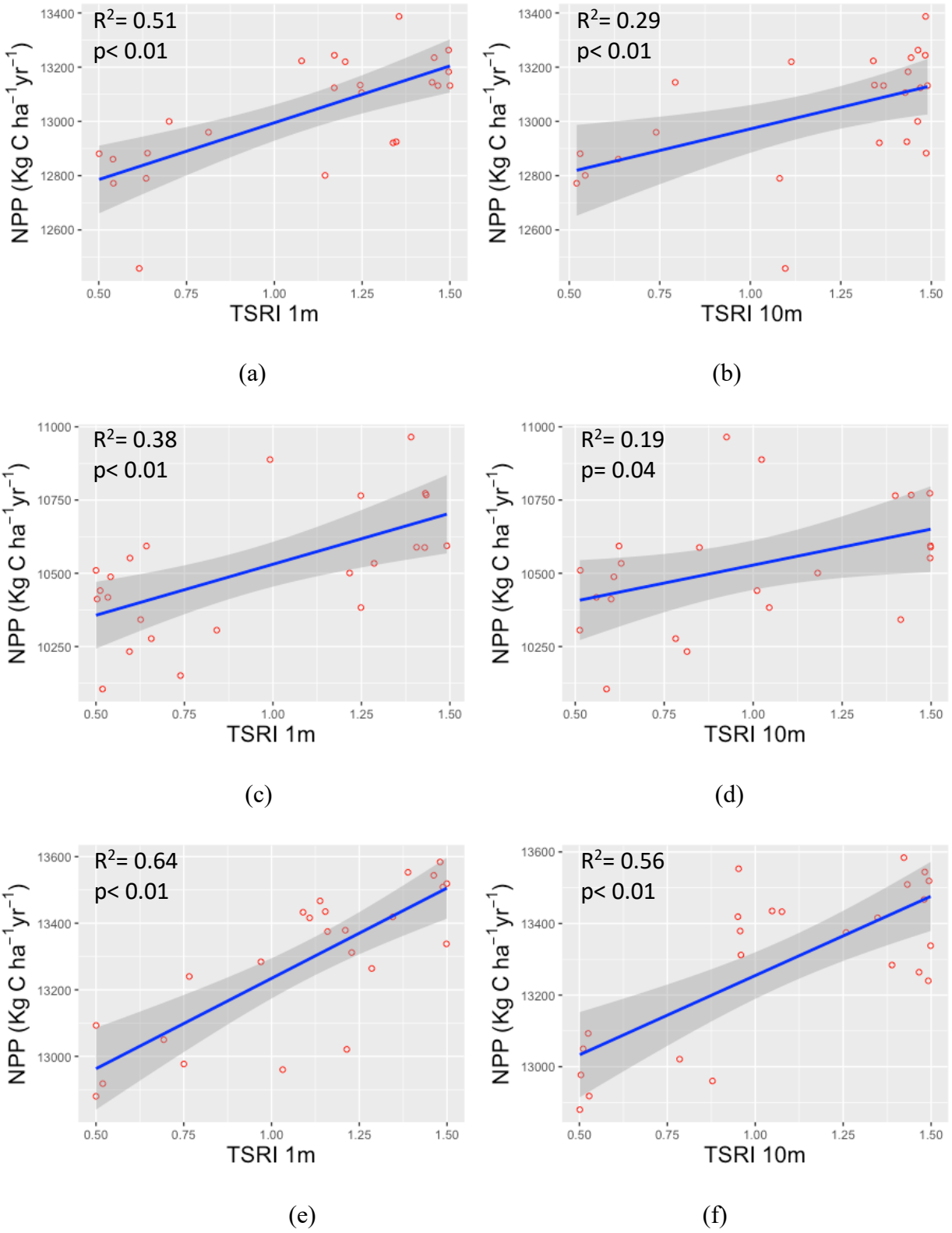

Figure 3.6: The relationship between (a) NPP and DTM-based TSRI in Deciduous Forest, (b) NPP and DEM-based TSRI in Deciduous Forest, (c) NPP and DTM-based TSRI in

Evergreen Forest, (d) NPP and DEM-based TSRI in Evergreen Forest, (e) NPP and DTM-based TSRI in Mixed Forest and (f) NPP and DEM-based TSRI in Mixed Forest.

The results showed that the relationship between NPP and TSRI derived from Airborne LiDAR DTM (1m*1m) is stronger than that calculated by National DEM (10m*10m) which indicated that the TSRI derived from high-resolution remote sensing data could better characterize the NPP variability at the regional scale.

3.6 Impact of forest stand age on NPP:

We derived the forest stand age maps for our two watersheds (Queets and Hoh) by using multi-temporal Landsat data coupled with VCT algorithm (see Section 2.6). The forest age maps for each class were produced by overlapping the stand age maps with NLCD.

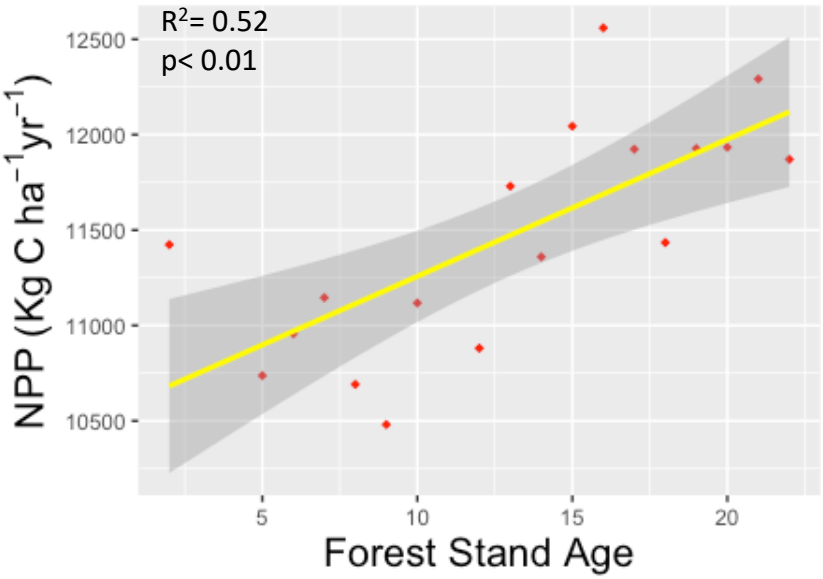

(a)

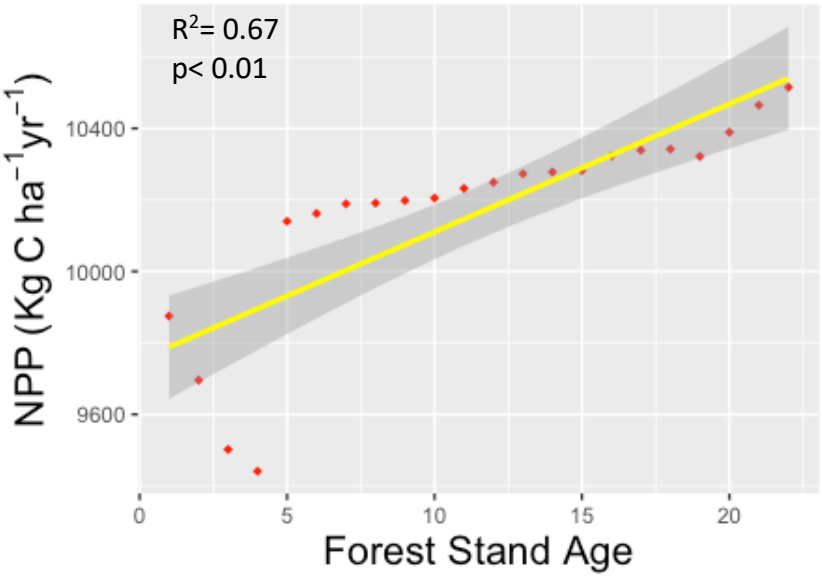

(b)

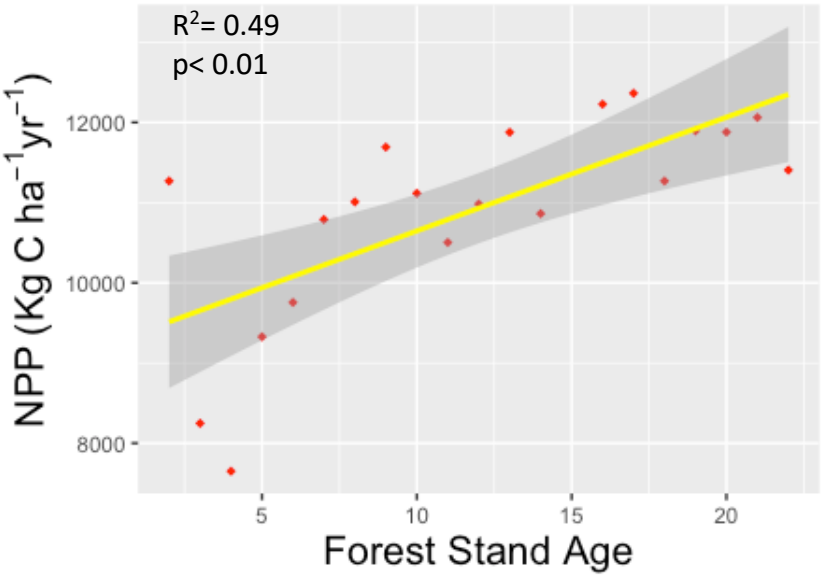

(c)

Figure 3.7: The relationship between NPP and forest stand age after disturbance in (a) Deciduous Forest, (b) Evergreen Forest and (c) Mixed Forest.

The NPP for each age group and forest type was calculated by averaging the NPP of all the pixels at the same age with the same forest cover types. The correlation between NPP and forest

stand age in different forest types are demonstrated in Figure 3.5. The linear increasing trends of annual NPP with increasing stand age were observed in all forest types. Notably, the NPP of Evergreen Forests slightly decreased before the steady increase, which was probably caused by forest competition or may possibly be just noise from the remotely sensed data.

Chapter 4: Discussion

Previous studies suggest that the process-based models were more reliable than statistical models probably because they simulated the biological processes impacting the NPP, which include photosynthesis, respiration and transpiration (Liu et al. 1997, Yang and Yu 2017). The results of ground-truthing validation in our study coincided with the previous research, demonstrating that process-based models can better characterize the NPP variability at the regional scale. However, large uncertainties still existed in NPP products simulated by process-based models including those introduced by upstream data input and model structure (Wang et al. 2017, Pan et al. 2006, Nightingale et al. 2007). There were many outliers because of the overestimation of MODIS-based NPP and these are shown in Figure 4.1(a). Specifically, the MOIDS-based NPP was frequently overestimated when the actual NPP was lower than $500g*m^{-1}*year^{-1}$, which could be potentially caused by the land-cover misclassification. A stronger linear relationship was observed when we removed the outliers, as shown in Figure 4.1(b). In order to clarify the cause of the outliers, we extracted the land-cover types of the outliers from NLCD and MODIS Land-cover product (MCD12Q1), as shown in Table 4.1.

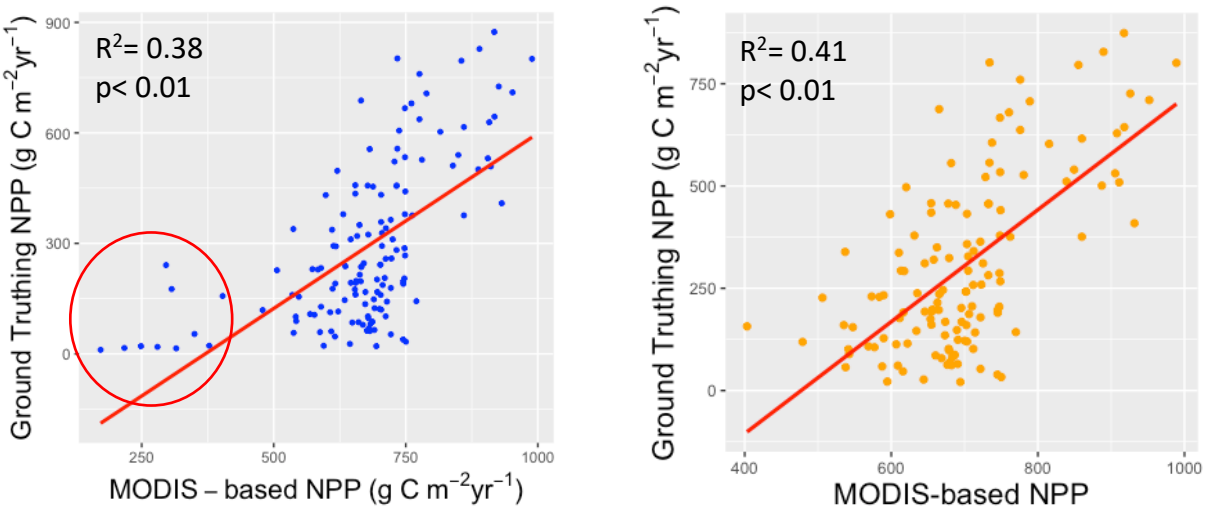

(a) **(b)**

Figure 4.1: The relationship between Ground truthing NPP and MODIS-based NPP with outliers (a) and without outliers (b).

Table 4.1: The Land-cover types of the outliers from NLCD and MCD12Q1.

Datasets / NPP values of outliers	MCD12Q1	NLCD
(11, 172.2)	Grassland	Shrub/ Scrub
(16, 217.2)	Grassland	Shrub/ Scrub
(21, 248.6)	Woody Savannas	Shrub/ Scrub
(19, 279.9)	Grassland	Shrub/ Scrub
(15, 315.3)	Grassland	Shrub/ Scrub
(22, 377.9)	Woody Savannas	Shrub/ Scrub
(54, 350)	Grassland	Shrub/ Scrub
(176, 306.7)	Grassland	Evergreen Forest
(241, 296.1)	Grassland	Evergreen Forest

The results showed that the land-cover types of the outliers were different in NLCD and MCD12Q1. Since the land-cover data was an important input of the Biome-BGC model for the

NPP simulation, the discrepancy of different land-cover types between Landsat- and MODIS-NPP products will potentially cause uncertainties.

Comparatively, the NPP product simulated by Landsat data and Biome-BGC model can better characterize the NPP variability at the regional scale, which indicated the importance of input datasets on NPP quantification. However, the LAI data applied in Landsat NPP product relies on the established relationship between LAI and Normalized Difference Vegetation Index (NDVI) (Junbang et al. 2014). However, the empirical relationship built at the local scale, and over a short time frame, have limited applicability at large spatial scales (Ganguly et al. 2012). Therefore, it is of great significance to generate the Landsat-based LAI product from regional to global spatial scales based on a physical algorithm (Ganguly et al. 2012).

Previous research studies have suggested that the NDVI derived from remotely sensed imagery was a significant indicator of vegetation productivity (Emma et al. 2017, Box, Holben and Kalb 1989), and the empirical model relating vegetation indices to NPP can be even more reliable than the light-use efficiency approach which contains huge errors due to the coarse-scale meteorological data input (Turner et al. 2005, Emma et al. 2017). In order to understand the sensitivity of spectral indices on NPP variability in highly-productive temperate rainforest, spectral indices were derived based on Landsat imageries described in Section 2.4.1. Our results show that the sensitivity of spectral indices to NPP strongly depends on Land-cover types. Therefore, building an empirical model purely based on the relationship between NPP and spectral indices may not be very reliable in temperate rainforests at a regional scale.

Table 4.2: The relationship between NPP and spectral indices derived from Landsat imagery.

	Band 3	Band 4	Band 5	MSAVI	EVI	NDMI	NDVI	SAVI	PCA 1
Deciduous Forest	0.25	0.12	0.50	0.54	0.55	0.43	0.34	0.53	0.45
Evergreen Forest	0.44	0.35	0.29	0.28	0.29	-0.09	-0.07	0.31	0.36
Mixed Forest	0.19	0.39	-0.03	-0.07	-0.04	-0.05	0.43	0.05	0.37

The long-term annual NPP in Queets plot and Hoh plot were statistically different based on the results of one-way ANOVA test as shown in Figure 3.4. Many potential drivers causing the NPP differences in two plots should be considered, including forest cover percentage, TSRI, Rumple Index, forest type and LAI. Previous studies have suggested that there is a strong positive correlation between NPP and forest cover percentage at the regional scale (Rodhouse et al. 2012). We observed that the forest cover percentage in Queets plot was lower than that in Hoh plot based on the NLCD, which potentially impacted the NPP difference. The TSRI in Queets plot and Hoh plot were also extracted from the TSRI map generated by Airborne LiDAR data (Figure 2.4.b) and the results showed the incident solar radiation in Hoh plot was much higher than that in Queets plot. Since the NPP was positively related to the incident solar radiation and its absorption co-efficiency (Liu et al. 1997), the higher TSRI, as would be expected, indicated a higher annual NPP in the Hoh plot. The higher Rumple Index generated by the Airborne LiDAR point cloud explained the canopy self-shadowing, which indicated more shadow created due to canopy complexity (Kane et al. 2008). We noticed the Rumple Index in Queets plot was much higher, meaning more shadow was created because of the canopy surface. This shadow slowed down the rate of carbon fixation, which was produced annually. In order to understand the impact of forest type differences on NPP variability, we then calculated the long-term mean annual NPP of each forest type within our two watersheds (Queets and Hoh), as shown in Figure

4.2. There was a huge difference in terms of annual NPP between evergreen forests and mixed forests. Finally, the annual LAI data in Queets plot and Hoh plot were acquired as shown in Figure 2.3(c). The mean LAI in Hoh plot, estimated from 2003 to 2017, was higher than that in the Queets plot, supporting our conclusion that the NPP in Queets plot is greater.

Table 4.3: The potential factors causing the NPP difference in Queets plot and Hoh plot.

	Queets plot	Hoh plot
Forest Cover Percentage	0.74	0.9
Topography (TSRI)	0.65	1.44
Self-shadowing (Rumple Index)	7.83	2.88
Forest Type	Evergreen Forest	Mixed Forest
Leaf Area Index (MOD15A3H)	3.56	3.98

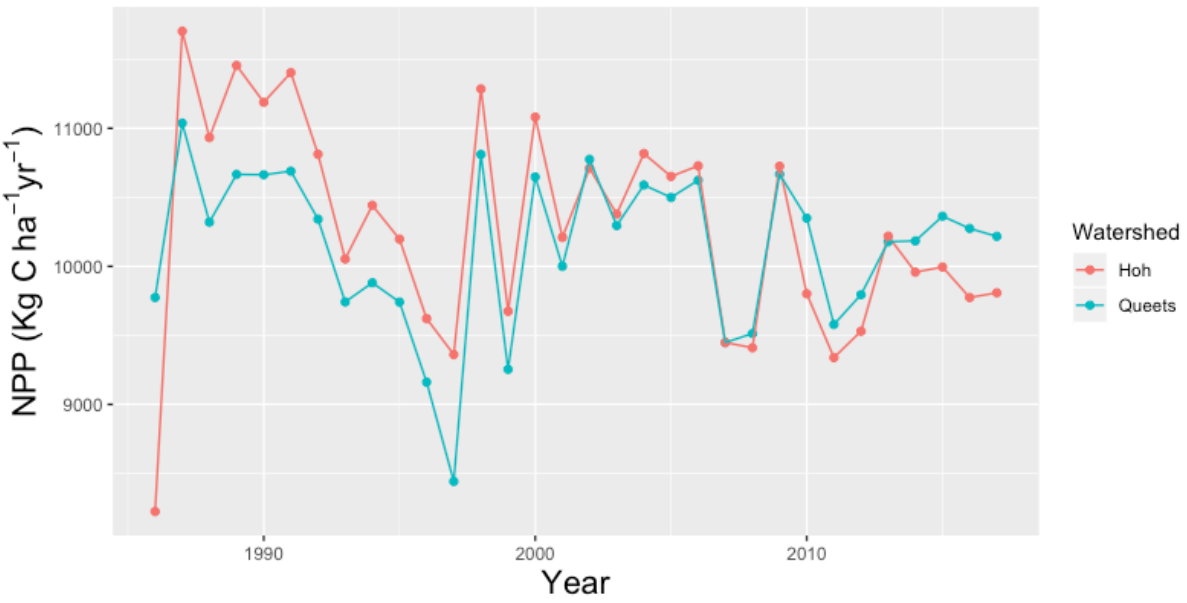

Figure 4.2: The long-term annual mean NPP in different forests within the two watersheds studied.

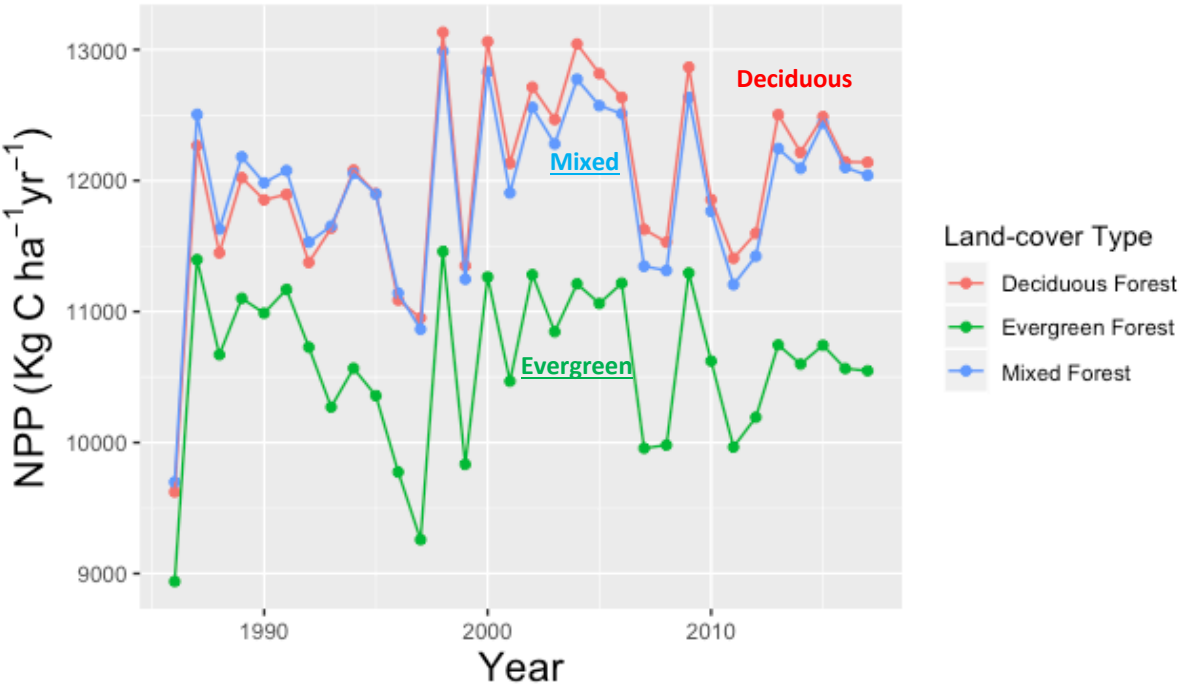

Figure 4.3: The long-term annual mean NPP trajectories in two watersheds of focus (Queets and Hoh) occurring between1986 and 2017.

The pixel-level metrics shown in Table 4.2 support our conclusion that the annual NPP in Hoh plot is higher than Queets plot. We then derived the long-term annual mean NPP trajectories in our two watersheds using the Google Earth Engine platform (Figure 4.3). We observed that the long-term annual mean NPP in our two watersheds were very close. This was potentially due to similar climatic conditions, species compositions and soil types. These results also demonstrates the importance of considering the geographic scale when determining the NPP variabilities.

Increasing trends were observed between annual NPP and stand age among all forest types (Section 3.5) at the regional scale. Due to the time span of the Landsat dataset, the forest stand age we derived ranged from 0 to 24 years. This limited our further exploration of the correlation between annual NPP and stand age of mature and old-growth stands.

In previous studies, similar trends were also observed when establishing the relationship between annual NPP and stand age by analyzing the stand yield data for black spruce in Ontario (Chen et al. 2002, Chen et al. 2003). The simulated NPP-age relationship for different site indices using a semi-empirical function is illustrated in Figure 4.5. We noticed that for black spruce, with age greater than 150 years, NPP gradually decreased for all site indexes but did not approach zero. It was suggested that the primary reason for the decrease was probably that the NPP for the old-growth black spruce stands was allocated almost exclusively to foliage and fine-root production with a short turn-over period (Chen et al. 2002). Therefore, the actual NPP-age relationship might be impacted by many potential factors including site condition, species composition and climate.

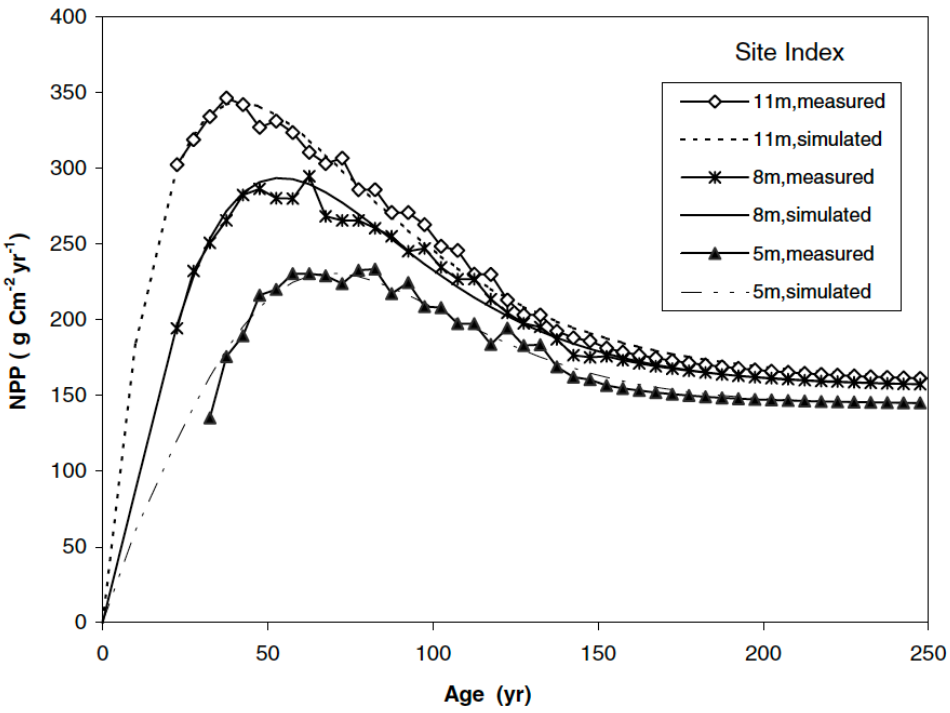

Figure 4.4: Simulated NPP-age relationship derived from black spruce stand yield data and Integrated Terrestrial Ecosystem Carbon (InTEC) model (Chen et al. 2003).

Future Research:

In this study, the accuracy of NPP products simulated by using the Biome-BGC model, with different input datasets, was tested by ground-truthing validation. The results suggested that the spatial resolution of input datasets played an important role in NPP simulation accuracy. Specifically, the Landsat-based NPP product showed a better correlation with the field-based data compared with the MODIS NPP data. However, discrepancies still existed between Landsat NPP data and ground-truthing data, which were caused by some other factors. The ground measurement errors will result in the disagreement and an accurate quantification of ground-truthing NPP will contribute to our understanding of each models performance. The plot-level NPP in this study was estimated based on the difference in biomass at two points in time divided by the number of intervening years between data collection (Law and Berner 2015). However, our study suggested that the rate of carbon accumulation by vegetation was closely related to the stand age. Therefore, the field-based NPP calculated by the ratio between biomass difference to the number of intervening years is the average NPP value between the two dates of data collection. Due to the short time interval between field data collection, we could approximate the average NPP value as the annual NPP of the year when the data were collected the second time even though there might be potential errors occurred. Another error source of ground measurement was from the sampling strategy. Specifically, we obtain the plot-level NPP by averaging the NPP of four different subplots encompassed by the plot with the size of one hectare. Therefore, potential errors could occur due to the 1) landscape heterogeneity, and 2) mismatched resolution of the NPP dataset. Due to the landscape heterogeneity, the NPP averaged by data collected in four subplots may not be able to well represent the NPP at the plot level due to the species composition and distribution of land-cover types. Secondly, the spatial size of field

plot was different from the MODIS NPP product so that the mismatched resolution will influence the underlying accuracy. In future research projects, improvements should be made to increase the accuracy of plot-level measurement including 1) appropriate selection of the dates of data collection and make sure the averaged NPP value represents the annual NPP, 2) carefully design the sample plot and match the spatial resolution of simulated NPP dataset, and 3) applying different NPP measurement approaches and calculate the NPP using Eddy Flux Tower. The precision of input dataset is also considered as one of the potential factors influencing the NPP simulation accuracy. In this study, the remotely sensed input for the Biome-BGC model include LAI, FPAR, NLCD. Both LAI and FPAR datasets were built upon the established empirical relationship with NDVI derived from Landsat Surface Reflectance data (Peng, Zhang and Liu 2012, Choudhury 1987). However, saturation effect was always observed when using passive remote sensing data for LAI quantification, meaning the LAI will not increase linearly due to the complex canopy structure such as foliage angular distribution (Zheng and Moskal 2009). The saturation effect will indirectly impact the accuracy of NPP simulation. Therefore, an improved approach for LAI and FPAR quantification will help us to better characterize the NPP variability across different spatial scales. Previous studies suggested the approaches of LAI calculation using LiDAR point cloud data will effectively overcome some of the disadvantages using passive remote sensing including cloud contamination and LAI saturation (Guang, Moskal and Soo-Hyung 2013, Zheng and Moskal 2009, Jensen et al. 2008, Bouvier et al. 2015, Tang et al. 2014, Moskal and Zheng 2012). Therefore, the use of LiDAR-based LAI as input parameter for NPP simulation should be implemented in the future research to verify the significance of precision of LAI on NPP simulation accuracy. Finally, some uncertainties were considered being introduced by model error. In original Biome-BGC model, the growth respiration was estimated

as a function of annual maximum LAI (Running and Zhao 2015). Therefore, the accuracy of growth respiration is affected by the maximum LAI value. However, the MODIS LAI product used for growth respiration calculation is under reflectance saturation condition when LAI is greater than 3, meaning the surface reflectance has low sensitivity to changing LAI (Myneni et al. 2002). As a consequence, the growth respiration in Biome-BGC model was then empirically parametrized as 25% of annual NPP (Ryan 1991, Cannell and Thornley 2000). Since the rate of growth respiration is influenced by different factors including plant species and external climate, the error might be introduced by constructing the empirical relationship between NPP and growth respiration. Therefore, the use of LiDAR-based LAI data can instead help us to accurately estimate the growth respiration, thus improving the model accuracy.

The TSRI generated by both Airborne LiDAR point cloud data and National DEM dataset were used in this study to investigate the impact of incident solar radiation on vegetation NPP variability in different types of forest within our two watersheds (Queets and Hoh). Our results suggested that the TSRI estimated by Airborne LiDAR data could better explain the NPP variation in our two watersheds due to its higher spatial resolution. However, some outliers were observed when a linear relationship was established between amount of incident solar radiation and annual NPP. This potentially could have been caused by 1) the imprecise quantification of incident solar radiation, and 2) the differences among vegetation traits in terms of the sensitivity to radiation energy. An accurate quantification of incident solar radiation is the precondition for understanding its influence on NPP variability. Therefore, some potential factors including atmospheric condition, solar zenith and azimuth angle should be considered in the future research in order to better understand the impact of radiation energy on vegetation NPP (Feng

and Wang 2018). In addition, a transformation from incident solar radiation to the Absorbed Photosynthetic Active Radiation (APAR) will benefit our understanding on how NPP is affected by radiation energy. Therefore, vegetation spectral signature and canopy structure should be incorporated for APAR calculation (Gitelson et al. 2015, Knyazikhin et al. 1998) in any future research to better explain the influence of radiation on NPP variability across different spatial scales.

Chapter 5: Summary

In this study, we explored the spatiotemporal patterns of vegetation NPP in our two watersheds using different models and investigated the impact of climate change and topography on NPP variability. Here we have summarized the main conclusions as follows:

1) The temperate rainforest in our study region was highly productive with annual NPP around 10,000 kg/ha/year.
2) The process-based model (Biome-BGC model) better explained the NPP variability in our two watersheds compared to the statistical models (Miami model and Thornthwaite Memorial model). By comparing the ground-truthing NPP dataset with the Landsat- and MODIS- NPP products, we concluded the spatial resolution of input data was closely linked to the NPP prediction accuracy.
3) There was a linear relationship between stand age and NPP for all forest types (Deciduous, Evergreen and Mixed Forest). Due to the time span of Landsat dataset, the forest stand ages derived in this study ranged from 0 to 24 years (young forest). With the increasing of stand age, the stand-level NPP was expected to decrease before reaching equilibrium.

4) Strong relationships were observed between NPP and LiDAR-based TSRI among all forest types, indicating the significance of solar radiation energy on plant carbon production. Comparatively, the National DEM-based TSRI cannot explain the NPP variability as well as LiDAR-based TSRI due to the relatively low spatial resolution.

Literature Cited:

Adams, B., A. White & T. M. Lenton (2004) An analysis of some diverse approaches to modelling terrestrial net primary productivity. *Ecological Modelling,* 177**,** 353-391.

Akaike, H. (1974) A new look at the statistical model identification. *IEEE Transactions on Automatic Control,* 19**,** 716-723.

Birdsey, R., K. Pregitzer & A. Lucier. 2006. Forest carbon management in the United States: 1600-2100. 1461-1469.

Bouvier, M., S. Durrieu, R. A. Fournier & J.-P. Renaud (2015) Generalizing predictive models of forest inventory attributes using an area-based approach with airborne LiDAR data. *Remote Sensing of Environment,* 156**,** 322-334.

Box, E. O., B. N. Holben & V. Kalb (1989) Accuracy of the AVHRR vegetation index as a predictor of biomass, primary productivity and net CO2 flux. *Vegetatio,* 80**,** 71-89.

Burnham, K. P. 2002. *Model selection and multimodel inference : a practical information-theoretic approach*. New York: New York : Springer.

Canadella, J. G. & M. R. Raupacha (2007) Contributions to accelerating atmospheric CO2 growth from economic activity, carbon intensity, and efficiency of natural sinks. *Proceedings of the National Academy of Sciences of the United States of America,* 104.

Cannell, M. G. R. & J. H. M. Thornley (2000) Modelling the components of plant respiration: Some guiding principles. *Annals of Botany,* 85**,** 45-54.

Change, I. C. 2007. The physical scientific basis. The Fourth Assessment Report of Working Group. Cambridge: Cambridge University Press.

Chapin, F. S. 2002. *Principles of terrestrial ecosystem ecology*. New York: New York : Springer.

Chen, J. M., W. Ju, J. Cihlar, D. Price, J. Liu, W. Chen, J. Pan, A. Black & A. Barr (2003) Spatial distribution of carbon sources and sinks in Canada's forests. *Tellus B,* 55**,** 622-641.

Chen, W., J. Chen & J. Cihlar (2000a) An integrated terrestrial ecosystem carbon-budget model based on changes in disturbance, climate, and atmospheric chemistry. *Ecological Modelling,* 135**,** 55-79.

Chen, W., J. Chen, J. Liu & J. Cihlar (2000b) Approaches for reducing uncertainties in regional forest carbon balance. *Global Biogeochemical Cycles,* 14**,** 827-838.

Chen, W., J. Chen, D. Price & J. Cihlar (2002) Effects of stand age on net primary productivity of boreal black spruce forests in Ontario, Canada. *Canadian Journal of Forest Research/Revue Canadienne de Recherche Forestiere,* 32**,** 833-842.

Choudhury, B. J. (1987) Relationships between vegetation indices, radiation absorption, and net photosynthesis evaluated by a sensitivity analysis. *Remote Sensing of Environment,* 22**,** 209-233.

Coulston, J., G. Moisen, B. Wilson, M. Finco, W. Cohen & C. Brewer (2012) Modeling Percent Tree Canopy Cover: A Pilot Study. *Photogrammetric Engineering and Remote Sensing,* 78**,** 715-727.

Coulston, J. W., D. M. Jacobs, C. R. King & I. C. Elmore (2013) The influence of multi-season imagery on models of canopy cover: A case study. *Photogrammetric Engineering and Remote Sensing,* 79**,** 469-477.

Daly, C., M. Halbleib, J. I. Smith, W. P. Gibson, M. K. Doggett, G. H. Taylor, J. Curtis & P. P. Pasteris (2008) Physiographically sensitive mapping of climatological temperature and precipitation across the conterminous United States. *International Journal of Climatology,* 28**,** 2031-2064.

Davis, S. C., A. E. Hessl, C. J. Scott, M. B. Adams & R. B. Thomas (2009) Forest carbon sequestration changes in response to timber harvest. *Forest Ecology and Management,* 258**,** 2101-2109.

DellaSala, D. A. 2011. *Temperate and boreal rainforests of the world : ecology and conservation*. Washington, DC: Washington, DC : Island Press.

Dixon, R. K., A. Solomon, S. Brown, R. Houghton, M. Trexier & J. J. S. Wisniewski (1994) Carbon pools and flux of global forest ecosystems. 263**,** 185-190.

Dubayah, R. & S. Loechel (1997) Modeling topographic solar radiation using GOES data. (Geostationary Operational Environmental Satellite). *Journal of Applied Meteorology,* 36**,** 141.

Emma, J. T., S. R. Clare, M. S. Simon, C. M. Lindsay & R. N. Lisa (2017) Regional-Scale High Spatial Resolution Mapping of Aboveground Net Primary Productivity (ANPP) from Field Survey and Landsat Data: A Case Study for the Country of Wales. *Remote Sensing,* 9**,** 801.

Fang, J., A. Chen, C. Peng, S. Zhao & L. J. S. Ci (2001) Changes in forest biomass carbon storage in China between 1949 and 1998. 292**,** 2320-2322.

Feng, F. & K. Wang (2018) Merging Satellite Retrievals and Reanalyses to Produce Global Long-Term and Consistent Surface Incident Solar Radiation Datasets. *Remote Sens.,* 10.

Ferguson, D. E., F. D. Johnson & P. Morgan. *Proceedings, land classifications based on vegetation : applications for resource management : Moscow, ID, November 17-19, 1987*. U.S. Dept. of Agriculture, Forest Service, Intermountain Research Station.

Fung, I. (2013) A Hyperventilating Biosphere. *Science,* 341**,** 1075-1076.

Ganguly, S., R. R. Nemani, G. Zhang, H. Hashimoto, C. Milesi, A. Michaelis, W. Wang, P. Votava, A. Samanta, F. Melton, J. L. Dungan, E. Vermote, F. Gao, Y. Knyazikhin & R. B. Myneni (2012) Generating global Leaf Area Index from Landsat: Algorithm formulation and demonstration. *Remote Sensing of Environment,* 122**,** 185-202.

Gao, B.-C. (1996) NDWI—A normalized difference water index for remote sensing of vegetation liquid water from space. *Remote Sensing of Environment,* 58**,** 257-266.

Geological, S. 1999. *National elevation dataset*. Reston, Va.?]: Reston, Va.? : U.S. Dept. of the Interior, U.S. Geological Survey.

Gesch, D., M. Oimoen, S. Greenlee, C. Nelson, M. Steuck & D. Tyler (2002) The National Elevation Dataset. *Photogrammetric Engineering and Remote Sensing,* 68**,** 5-11.
Gitelson, A. A., Y. Peng, T. J. Arkebauer & A. E. Suyker (2015) Productivity, absorbed photosynthetically active radiation, and light use efficiency in crops: Implications for remote sensing of crop primary production. *Journal of Plant Physiology,* 177**,** 100-109.
Gmur, S., D. Vogt, D. Zabowski & L. M. Moskal (2012) Hyperspectral Analysis of Soil Nitrogen, Carbon, Carbonate, and Organic Matter Using Regression Trees. 12**,** 10639-10658.
Gmur, S. J., D. J. Vogt, K. A. Vogt & A. S. Suntana (2014) Effects of different sampling scales and selection criteria on modelling net primary productivity of Indonesian tropical forests. 41**,** 187-197.
Goward, S., C. Huang, J. Masek, W. Cohen, G. Moisen & K. J. O. D. Schleeweis (2012) NACP North American Forest Dynamics Project: Forest Disturbance and Regrowth Data.
Goward, S. N., J. G. Masek, W. Cohen, G. Moisen, G. J. Collatz, S. Healey, R. Houghton, C. Huang, R. Kennedy & B. J. E. Law, Transactions American Geophysical Union (2008) Forest disturbance and North American carbon flux. 89**,** 105-106.
Guang, Z., L. M. Moskal & K. Soo-Hyung (2013) Retrieval of Effective Leaf Area Index in Heterogeneous Forests With Terrestrial Laser Scanning. *IEEE Transactions on Geoscience and Remote Sensing,* 51**,** 777-786.
Hao, W., L. Guohua, L. Zongshan, W. Pengtao & W. Zhuangzhuang (2018) Assessing the Driving Forces in Vegetation Dynamics Using Net Primary Productivity as the Indicator: A Case Study in Jinghe River Basin in the Loess Plateau. *Forests,* 9**,** 374.
Henderson, J. A. & R. United States. Forest Service. Pacific Northwest. 1989. Forested plant associations of the Olympic National Forest. Portland, Or.]: Portland, Or. : USDA, Forest Service, Pacific Northwest Region.
Homer, C., J. Dewitz, L. Yang, S. Jin, P. Danielson, G. Xian, J. Coulston, N. Herold, J. Wickham & K. Megown (2015) Completion of the 2011 National Land Cover Database for the Conterminous United States – Representing a Decade of Land Cover Change Information. *Photogrammetric Engineering & Remote Sensing,* 81**,** 345-354.
Huang, C., GOWARD, N. Samuel, MASEK, G. Jeffrey, THOMAS, Nancy, Z. Zhu, VOGELMANN & E. J. R. S. o. E. James (2010) An automated approach for reconstructing recent forest disturbance history using dense Landsat time series stacks. 114**,** 183-198.
Huang, C., S. N. Goward, J. G. Masek, F. Gao, E. F. Vermote, N. Thomas, K. Schleeweis, R. E. Kennedy, Z. Zhu, J. C. Eidenshink & J. R. G. Townshend (2009) Development of time series stacks of Landsat images for reconstructing forest disturbance history. *International Journal of Digital Earth,* 2**,** 195-218.
Huete, A., K. Didan, T. Miura, E. P. Rodriguez, X. Gao & L. G. Ferreira (2002) Overview of the radiometric and biophysical performance of the MODIS vegetation indices. *Remote Sensing of Environment,* 83**,** 195-213.
Huete, A. R. (1988) A soil-adjusted vegetation index (SAVI). *Remote Sensing of Environment,* 25**,** 295-309.
James, E. V., K. Phung Van, L. Do Xuan, S. Jacob, S. Hua, C. W. Michael, D. Hoang Tat & H. Le Van (2017) Assessment of Forest Degradation in Vietnam Using Landsat Time Series Data. *Forests,* 8**,** 238.

Jensen, J. L. R., K. S. Humes, L. A. Vierling & A. T. Hudak (2008) Discrete return lidar-based prediction of leaf area index in two conifer forests. *Remote Sensing of Environment,* 112**,** 3947-3957.

Junbang, W., D. Jingwei, L. Jiyuan, H. Mei, L. Guicai, W. R. Steven, W. K. Smith, H. Warwick, S. Nobuko, K. Hiroaki, L. Yunfen, H. Takashi & X. Xiangming (2014) Comparison of Gross Primary Productivity Derived from GIMMS NDVI3g, GIMMS, and MODIS in Southeast Asia. *Remote Sensing,* 6**,** 2108-2133.

Kane, V. R., A. R. Gillespie, R. McGaughey, J. A. Lutz, K. Ceder & J. F. Franklin (2008) Interpretation and topographic compensation of conifer canopy self-shadowing. *Remote Sensing of Environment,* 112**,** 3820-3832.

Kashian, D. M., W. H. Romme, D. B. Tinker, M. G. Turner & M. G. Ryan (2006) Carbon Storage on Landscapes with Stand-replacing Fires. *BioScience,* 56**,** 598-606.

Keith, H., B. G. Mackey & D. B. Lindenmayer (2009) Re-evaluation of forest biomass carbon stocks and lessons from the world's most carbon-dense forests. *Proceedings of the National Academy of Sciences of the United States of America,* 106**,** 11635.

Knyazikhin, Y., J. Martonchik, R. Myneni, D. Diner & S. Running (1998) Synergistic algorithm for estimating vegetation canopy leaf area index and fraction of absorbed photosynthetically active radiation from MODIS and MISR data. *Journal of Geophysical Research: Atmospheres,* 103**,** 32257-32275.

Landres, P. B., P. Morgan & F. J. Swanson (1999) OVERVIEW OF THE USE OF NATURAL VARIABILITY CONCEPTS IN MANAGING ECOLOGICAL SYSTEMS. *Ecological Applications,* 9**,** 1179-1188.

Law, B. E. & L. T. Berner. 2015. NACP TERRA-PNW: Forest Plant Traits, NPP, Biomass, and Soil Properties, 1999-2014. ORNL Distributed Active Archive Center.

Lewis, J. C., K. J. Jenkins, P. J. Happe, D. J. Manson & M. McCalmon (2016) Landscape-scale habitat selection by fishers translocated to the Olympic Peninsula of Washington. *Forest Ecology and Management,* 369**,** 170-183.

Liang, W., Y. Yang, D. Fan, H. Guan, T. Zhang, D. Long, Y. Zhou & D. Bai (2015) Analysis of spatial and temporal patterns of net primary production and their climate controls in China from 1982 to 2010. *Agricultural and Forest Meteorology,* 204**,** 22-36.

Lieth, H. 1975. Modeling the primary productivity of the world. In *Primary productivity of the biosphere*, 237-263. Springer.

Lin, Z. & R. J. C. C. Zhang (2012) Effects of climate change and elevated atmospheric CO2 on soil organic carbon: a response equation. 113**,** 107-120.

Liu, J., J. M. Chen, J. Cihlar & W. Chen (2002) Net primary productivity mapped for Canada at 1-km resolution. *Global Ecology and Biogeography,* 11**,** 115-129.

Liu, J., J. M. Chen, J. Cihlar & W. M. Park (1997) A process-based boreal ecosystem productivity simulator using remote sensing inputs. *Remote Sensing of Environment,* 62**,** 158-175.

Lomolino, M. V. & D. R. Perault (2007) Body Size Variation of Mammals in a Fragmented, Temperate Rainforest

Variación del Tamaño del Cuerpo de Mamíferos en un Bosque Lluvioso Templado, Fragmentado. *Conservation Biology,* 21**,** 1059-1069.

Masek, J. G., E. F. Vermote, N. E. Saleous, R. Wolfe, F. G. Hall, K. F. Huemmrich, G. Feng, J. Kutler & L. Teng-Kui (2006) A Landsat surface reflectance dataset for North America, 1990-2000. *Geoscience and Remote Sensing Letters, IEEE,* 3**,** 68-72.

Michaletz, S., D. Cheng, A. Kerkhoff & B. Enquist (2014) Convergence of terrestrial plant production across global climate gradients. *Nature,* 512**,** 39-43.
Mildrexler, D. J., M. Zhao, F. A. Heinsch & S. W. Running (2007) A NEW SATELLITE-BASED METHODOLOGY FOR CONTINENTAL-SCALE DISTURBANCE DETECTION. *Ecological Applications,* 17**,** 235-250.
Moskal, L. M. & M. E. Jakubauskas (2013) Monitoring Post Disturbance Forest Regeneration with Hierarchical Object-Based Image Analysis. 4**,** 808-829.
Moskal, L. M. & G. Zheng (2012) Retrieving Forest Inventory Variables with Terrestrial Laser Scanning (TLS) in Urban Heterogeneous Forest. 4**,** 1-20.
Mu, S., S. Zhou, Y. Chen, J. Li, W. Ju & I. O. A. Odeh (2013) Assessing the impact of restoration-induced land conversion and management alternatives on net primary productivity in Inner Mongolian grassland, China. *Global and Planetary Change,* 108**,** 29-41.
Myneni, R., Y. Knyazikhin & T. J. N. E. L. P. D. Park (2015) MOD15A2H MODIS/terra leaf area index/FPAR 8-day L4 global 500 m SIN grid V006.
Myneni, R. B., S. Hoffman, Y. Knyazikhin, J. L. Privette, J. Glassy, Y. Tian, Y. Wang, X. Song, Y. Zhang, G. R. Smith, A. Lotsch, M. Friedl, J. T. Morisette, P. Votava, R. R. Nemani & S. W. Running (2002) Global products of vegetation leaf area and fraction absorbed PAR from year one of MODIS data. *Remote Sensing of Environment,* 83**,** 214-231.
Nadkarni, N. M. (1984) Biomass and mineral capital of epiphytes in an Acer macrophyllum community of a temperate moist coniferous forest, Olympic Peninsula, Washington State. *Canadian Journal of Botany,* 62**,** 2223-2228.
Nightingale, J. M., N. C. Coops, R. H. Waring & W. W. Hargrove (2007) Comparison of MODIS gross primary production estimates for forests across the U.S.A. with those generated by a simple process model, 3-PGS. *Remote Sensing of Environment,* 109**,** 500-509.
Pan, Y., R. Birdsey, J. Hom, K. McCullough & K. Clark (2006) Improved Estimates Of Net Primary Productivity From MODIS Satellite Data At Regional And Local Scales. *Ecological Applications,* 16**,** 125-132.
Parker, G. G., M. E. Harmon, M. A. Lefsky, J. Chen, R. V. Pelt, S. B. Weis, S. C. Thomas, W. E. Winner, D. C. Shaw & J. F. Frankling (2004) Three-dimensional Structure of an Old-growth Pseudotsuga-Tsuga Canopy and Its Implications for Radiation Balance, Microclimate, and Gas Exchange. *Ecosystems,* 7**,** 440-453.
Peel, M. C., B. L. Finlayson & T. A. McMahon (2007) Updated world map of the Köppen-Geiger climate classification. *Hydrology and Earth System Sciences,* 11**,** 1633-1644.
Peng, D., B. Zhang & L. Liu (2012) Comparing spatiotemporal patterns in Eurasian FPAR derived from two NDVI-based methods. *International Journal of Digital Earth,* 5**,** 283-298.
Peng, S., A. Chen, L. Xu, C. Cao, J. Fang, R. B. Myneni, J. E. Pinzon, C. J. Tucker & S. Piao (2011) Recent change of vegetation growth trend in china. *Environmental Research Letters,* 6**,** 044027.
Pons, X. & M. Ninyerola (2008) Mapping a topographic global solar radiation model implemented in a GIS and refined with ground data. *International Journal of Climatology,* 28**,** 1821-1834.
Potter, C., S. Klooster, V. Genovese & C. Hiatt (2013) Forest production predicted from satellite image analysis for the Southeast Asia region. *Carbon Balance and Management,* 8.

Potter, C. S., S. A. Klooster & P. A. Matson (1993) Terrestrial ecosystem production: A process model based on global satellite and surface data. *Global Biogeochemical Cycles,* 7.
Qi, J., A. Chehbouni, A. R. Huete, Y. H. Kerr & S. Sorooshian (1994) A modified soil adjusted vegetation index. *Remote Sensing of Environment,* 48**,** 119-126.
Rice, C. W. (2006) Introduction to special section on greenhouse gases and carbon sequestration in agriculture and forestry. *Journal of Environmental Quality,* 35**,** 1338-1340.
Robinson, N. P., B. W. Allred, W. K. Smith, M. O. Jones, A. Moreno, T. A. Erickson, D. E. Naugle & S. W. Running (2018) Terrestrial primary production for the conterminous United States derived from Landsat 30 m and MODIS 250 m. *Remote Sensing in Ecology and Conservation,* 4**,** 264-280.
Rodhouse, T. J., P. C. Ormsbee, K. M. Irvine, L. A. Vierling, J. M. Szewczak & K. T. Vierling (2012) Assessing the status and trend of bat populations across broad geographic regions with dynamic distribution models. *Ecological Applications,* 22**,** 1098-1113.
Rouse, J. W., Jr. 1973. Monitoring the vernal advancement and retrogradation (green wave effect) of natural vegetation - NASA-CR-133531.
Ruimy, A., B. Saugier & G. Dedieu (1994) Methodology for the estimation of terrestrial net primary production from remotely sensed data. *Journal of Geophysical Research: Atmospheres,* 99**,** 5263-5283.
Running, S. W. & M. J. M. U. s. G. Zhao (2015) Daily GPP and annual NPP (MOD17A2/A3) products NASA Earth Observing System MODIS land algorithm. 2015.
Ryan, M. G. (1991) Effects of Climate Change on Plant Respiration. *Ecological Applications,* 1**,** 157-167.
Schuur, E. A. G. (2003) PRODUCTIVITY AND GLOBAL CLIMATE REVISITED: THE SENSITIVITY OF TROPICAL FOREST GROWTH TO PRECIPITATION. *Ecology,* 84**,** 1165-1170.
Schwörer, C., D. M. Fisher, D. G. Gavin, C. Temperli & P. J. Bartlein (2016) Modeling postglacial vegetation dynamics of temperate forests on the Olympic Peninsula (WA, USA) with special regard to snowpack. *Climatic Change,* 137**,** 379-394.
Sebastiaan, L., E. D. Schulze, B. Annett, K. Alexander, H. Dominik, E. L. Beverly, C. Philippe & G. John (2008) Old- growth forests as global carbon sinks. *Nature,* 455**,** 213.
Smithwick, E. A. H., M. E. Harmon, S. M. Remillard, S. A. Acker & J. F. Franklin (2002) POTENTIAL UPPER BOUNDS OF CARBON STORES IN FORESTS OF THE PACIFIC NORTHWEST. *Ecological Applications,* 12**,** 1303-1317.
Tang, H., M. Brolly, F. Zhao, A. H. Strahler, C. L. Schaaf, S. Ganguly, G. Zhang & R. Dubayah (2014) Deriving and validating Leaf Area Index (LAI) at multiple spatial scales through lidar remote sensing: A case study in Sierra National Forest, CA. *Remote Sensing of Environment,* 143**,** 131-141.
Toms, J. D. & M. L. Lesperance (2003) PIECEWISE REGRESSION: A TOOL FOR IDENTIFYING ECOLOGICAL THRESHOLDS. *Ecology,* 84**,** 2034-2041.
Turner, D. P., W. D. Ritts, W. B. Cohen, T. K. Maeirsperger, S. T. Gower, A. A. Kirschbaum, S. W. Running, M. Zhao, S. C. Wofsy, A. L. Dunn, B. E. Law, J. L. Campbell, W. C. Oechel, H. J. Kwon, T. P. Meyers, E. E. Small, S. A. Kurc & J. A. Gamon (2005) Site-level evaluation of satellite-based global terrestrial gross primary production and net primary production monitoring. *Global Change Biology,* 11**,** 666-684.

Vogt, D. J., K. A. Vogt, S. J. Gmur, J. J. Scullion, A. S. Suntana, S. Daryanto & R. Sigurðardóttir (2016) Vulnerability of tropical forest ecosystems and forest dependent communities to droughts. *Environmental Research,* 144**,** 27-38.

Vogt, K.A., J. Gordon, J. Wargo, D.J. Vogt, H. Asbjornsen, P.A. Palmiotto, H. Clark, J. O'Hara, W.S. Keeton, & T. Patel-Weynand (1996) Ecosystems: Balancing Science with Management. With contributions by E. Witten, B. Larson, D. Tortoriello, J. Perez, A. Marsh, M. Corbett, K. Kaneda, F. Meyerson, and D. Smith. Springer-Verlag. 470 pp.

Vogt K.A., T. Patel-Weynand, M. Shelton, D.J. Vogt, J.C. Gordon, C.T. Mukumoto, A.S. Suntana, & P.A. Roads (2010) Sustainability Unpacked: Food, Energy and Water for Resilient Environments and Societies. Earthscan. London, Washington DC. 305 pp.

Wang, B., M. Li, W. Fan, Y. Yu & J. Chen (2018) Relationship between Net Primary Productivity and Forest Stand Age under Different Site Conditions and Its Implications for Regional Carbon Cycle Study. *Forests,* 9**,** 5.

Wang, J., J. Dong, Y. Yi, G. Lu, J. Oyler, W. K. Smith, M. Zhao, J. Liu & S. Running (2017) Decreasing net primary production due to drought and slight decreases in solar radiation in China from 2000 to 2012. *Journal of Geophysical Research: Biogeosciences,* 122**,** 261-278.

Wang, S., L. Zhou, J. Chen, W. Ju, X. Feng & W. Wu (2011) Relationships between net primary productivity and stand age for several forest types and their influence on China's carbon balance. *Journal of Environmental Management,* 92**,** 1651-1662.

Wang, W., X. Wei, W. Liao, J. A. Blanco, Y. Liu, S. Liu, G. Liu, L. Zhang, X. Guo & S. Guo (2012) Evaluation of the effects of forest management strategies on carbon sequestration in evergreen broad-leaved (Phoebe bournei) plantation forests using FORECAST ecosystem model. *Forest Ecology and Management,* 300.

Wen, Y., X. Liu & G. Du (2018) Nonuniform Time-Lag Effects of Asymmetric Warming on Net Primary Productivity across Global Terrestrial Biomes. *Earth Interactions,* 22**,** 1-26.

Wen, Z., S. Wu, J. Chen & M. Lü (2017) NDVI indicated long-term interannual changes in vegetation activities and their responses to climatic and anthropogenic factors in the Three Gorges Reservoir Region, China. *Science of the Total Environment,* 574**,** 947-959.

Wenjuan, S., L. Mingshi, H. Chengquan & W. Anshi (2016) Quantifying Live Aboveground Biomass and Forest Disturbance of Mountainous Natural and Plantation Forests in Northern Guangdong, China, Based on Multi-Temporal Landsat, PALSAR and Field Plot Data. *Remote Sensing,* 8**,** 595.

Xu, G., H. Zhang, B. Chen, H. Zhang, J. Innes, G. Wang, J. Yan, Y. Zheng, Z. Zhu & R. Myneni (2014) Changes in Vegetation Growth Dynamics and Relations with Climate over China's Landmass from 1982 to 2011. *Remote Sensing,* 6**,** 3263-3283.

Yang, J. & X. Yu (2017) Nonlinear Variations of Net Primary Productivity and Its Relationship with Climate and Vegetation Phenology, China. *Forests,* 8**,** 361.

Yang, L., S. Jin, P. Danielson, C. Homer, L. Gass, S. M. Bender, A. Case, C. Costello, J. Dewitz, J. Fry, M. Funk, B. Granneman, G. C. Liknes, M. Rigge & G. Xian (2018) A new generation of the United States National Land Cover Database: Requirements, research priorities, design, and implementation strategies. *ISPRS Journal of Photogrammetry and Remote Sensing,* 146**,** 108-123.

Zaks, D. P. M., N. Ramankutty, C. C. Barford & J. A. Foley (2007) From Miami to Madison: Investigating the relationship between climate and terrestrial net primary production. *Global Biogeochemical Cycles,* 21**,** n/a-n/a.

Zhang, F., J. M. Chen, Y. Pan, R. A. Birdsey, S. Shen, W. Ju & L. He (2012) Attributing carbon changes in conterminous U.S. forests to disturbance and non-disturbance factors from 1901 to 2010. *Journal of Geophysical Research: Biogeosciences,* 117**,** n/a-n/a.

Zheng, G. & L. Moskal (2009) Retrieving Leaf Area Index (LAI) Using Remote Sensing: Theories, Methods and Sensors. *Sensors,* 9**,** 2719-2745.

Zhou, J., W. Cai, Y. Qin, L. Lai, T. Guan, X. Zhang, L. Jiang, H. Du, D. Yang, Z. Cong & Y. Zheng (2016) Alpine vegetation phenology dynamic over 16 years and its covariation with climate in a semi-arid region of China. *Science of the Total Environment,* 572**,** 119-128.

Zhou, W., C. Gang, F. Zhou, J. Li, X. Dong & C. Zhao (2015) Quantitative assessment of the individual contribution of climate and human factors to desertification in northwest China using net primary productivity as an indicator. *Ecological Indicators,* 48**,** 560-569.